

1 **Influence of Cloud Retrieval Errors Due to Three Dimensional Radiative Effects on**
2 **Calculations of Broadband Shortwave Cloud Radiative Effect**

3 Adeleke S. Ademakinwa^{1,2}, Zahid H. Tushar³, Jianyu Zheng^{1,2}, Chenxi Wang^{2,4}, Sanjay
4 Purushotham³, Jianwu Wang³, Kerry G. Meyer⁴, Tamas Várnai^{2,4}, Zhibo Zhang^{1,2,*}

- 5 1. Physics Department, University of Maryland Baltimore County (UMBC)
6 2. Goddard Earth Sciences Technology and Research (GESTAR) II, UMBC
7 3. Department of Information Systems, UMBC
8 4. Climate and Radiation Laboratory Code 613, NASA Godard Space Flight Center

9 *Corresponding author: Zhibo Zhang, zhibo.zhang@umbc.edu

10

11

Abstract

12 We investigate how cloud retrieval errors due to the three-dimensional (3D) radiative effects affect
13 broadband shortwave (SW) cloud radiative effects (CRE) in shallow cumulus clouds. A framework based
14 on the combination of large eddy simulations (LES) and radiative transfer (RT) models was developed to
15 simulate both one-dimensional (1D) and 3D radiance, and SW broadband fluxes. Results show that the
16 broadband SW fluxes reflected at top-of-the-domain, transmitted at the surface, and absorbed in the
17 atmosphere, computed from the cloud retrievals using 1D RT (F_{1D}^*) can provide reasonable broadband
18 radiative energy estimates in comparison with those derived from the true cloud fields using 1D RT (F_{1D}).
19 The difference between these 1D RT simulated fluxes (F_{1D}^* , F_{1D}) and the benchmark 3D RT simulations
20 computed from the true cloud field (F_{3D}), depends primarily on the horizontal transport of photons in 3D
21 RT, whose characteristics vary with the sun's geometry. When the solar zenith angle (SZA) is 5° , the
22 domain-averaged F_{1D}^* are in excellent agreement with the F_{3D} , all within 7% relative CRE bias. When the
23 SZA is 60° , the CRE differences between calculations from F_{1D}^* and F_{3D} are determined by how the cloud
24 side-brightening and darkening effects offset each other in the radiance, retrieval, and broadband fluxes.
25 This study suggests that although the cloud property retrievals based on the 1D RT theory may be biased
26 due to the 3D radiative effects, they still provide CRE estimates that are comparable to or better than CRE
27 calculated from the true cloud properties using 1D RT.

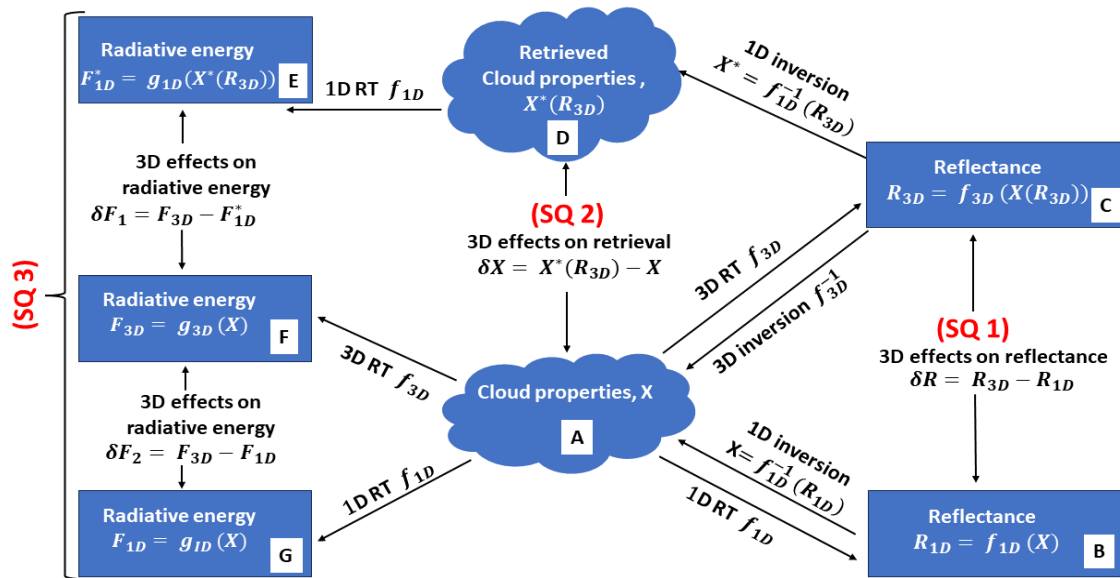
28 1. Introduction

29 Covering about 60-70% of the Earth's surface [Rossow and Schiffer, 1999; Vardavas and Taylor,
30 2011], clouds play a very important role in the Earth's climate system. Clouds can cool the Earth by
31 reflecting shortwave (SW) solar radiative flux back to space and at the same time warm the Earth by
32 retaining the outgoing longwave (LW) infrared radiative flux at the top of the atmosphere (TOA), known
33 as the cloud radiative effects (CRE). The annual global average TOA CRE is approximately -50 Wm^{-2} at
34 SW and 30 Wm^{-2} at LW, resulting in a net CRE of about -20 Wm^{-2} [Stocker, 2013]. These strong CRE
35 show that clouds greatly affect the Earth's energy budget [Ramanathan et al., 1989; Kiehl and Trenberth,
36 1997; Trenberth et al., 2009]. The CRE of clouds is largely determined by the optical and microphysical
37 properties of clouds including the cloud optical thickness (τ), cloud droplet effective radius (r_e), and cloud
38 liquid water path (LWP). Thus, continuous measurements of these cloud properties from regional to global
39 scales are critical to better understand the role of clouds in the climate systems. Currently, satellite based
40 remote sensing is the only way to make such observations. Remotely "retrieved" cloud properties based
41 on these satellite observations are often used to derive the radiative effects of clouds [e.g., Wielicki et al.,
42 1996; Platnick et al., 2003; Loeb and Manalo-Smith, 2005; Oreopoulos et al., 2016] and evaluate the
43 simulations of Earth System Models (ESMs) [Kay et al., 2012; Nam et al., 2012; Song et al., 2018].

44 A commonly used retrieval technique in passive satellite remote sensing is the bi-spectral retrieval
45 method first developed by Nakajima and King [1990]. It retrieves τ and r_e simultaneously from a pair of
46 total reflectance measurements, one from the non-absorbing visible or near infrared (VNIR) band (e.g.,
47 $0.66 \mu\text{m}$) and the other from the moderately absorbing short-wave infrared (SWIR) band (e.g., $2.13 \mu\text{m}$).
48 Since clouds in reality have three-dimensional (3D) structures, the simulation of radiative transfer (RT) in
49 clouds should ideally consider the transport of radiation in both vertical and horizontal directions (referred
50 to as "3D RT"). Unfortunately, the computational cost for 3D RT is extremely high. As a result, the
51 operational bi-spectral cloud retrievals are almost exclusively based on the one-dimensional (1D) RT
52 theory that considers only the vertical and ignores the net horizontal transport of radiation. The radiative
53 properties of clouds under 3D RT are substantially different from those under 1D RT. This is known as the
54 3D radiative effects and can lead to substantial biases in the cloud property retrievals based on 1D RT
55 [Várnai et al., 2001; Marshak et al., 2006; Zhang et al. 2012; Zhang et al. 2016]. Although recent efforts
56 have been made to employ machine learning techniques to retrieve cloud properties based on 3D RT
57 theory [Okamura et al., 2017; Masuda et al., 2019; Nataraja et al., 2022], these machine-learning based
58 algorithms are still in their infancy and far from being used in operational algorithms.

59 Many previous studies have investigated the 3D radiative effects on satellite radiance
60 observations and cloud property retrievals. For example, Welch and Wielicki [1984] used some "toy" cloud
61 fields (e.g., cubic, and cylindrical) to illustrate the impact of side-illuminating and mutual shadowing on
62 cloud albedo. Várnai and Davis [1999] and Várnai [2000] elucidated several 3D RT mechanisms, e.g.,
63 upward/downward trapping/escaping, that can result in significant differences between 1D and 3D cloud
64 albedo. Hogan et al. [2019] proposed a distinct mechanism, named "entrapment" which play a key role in
65 the 3D radiative effect of clouds. Davis and Marshak [2001] pointed out that the channeling effect in 3D
66 RT can smoothen out the small-scale cloud variations and lead to the reduction of cloud brightness at
67 cloud edges. Marshak et al. [2006] explained how the radiance biases due to 3D radiative effects can lead
68 to τ and r_e retrieval biases in MODIS (Moderate Resolution Imaging Spectroradiometer) cloud products.
69 This study is built upon these classic papers but has a different objective.

70 Here, we investigate an important question: Do cloud property retrievals based on 1D RT, which
71 are potentially biased due to the 3D radiative effects, still provide an observational basis to estimate the
72 broadband SW CRE? This is an important question because as mentioned above, operational cloud
73 retrieval products from, for example MODIS, are frequently used for CRE estimation and ESM evaluation.
74 However, to our best knowledge, the impacts of retrieval bias due to the 3D radiative effects on such
75 applications have never been examined systematically in previous studies. To better explain our objective
76 and the difference of this study from many previous ones on the 3D radiative effects, we need to introduce
77 a framework illustrated in **Fig. 1**. As conceptually illustrated in **Fig. 1**, the observed radiances are inherently
78 3D (i.e., from Box A to C) because the RT in nature is 3D. However, when 1D RT theory is used to interpret
79 the observations, we get the “retrieved cloud properties” in Box D that can be significantly different from
80 the “true” cloud properties in Box A. Although the retrieved cloud properties are often biased due to the
81 3D radiative effects, they are still widely used to compute the radiative fluxes by clouds (i.e., from Box D
82 to E) using 1D RT and the results are often used for studying the climatic effects of clouds [e.g., Kato et al.,
83 2011; Zelinka et al., 2012; Oreopoulos et al., 2016]. In contrast, the “true” radiative fluxes in nature are
84 also 3D (i.e., from Box A to F). A few recent studies have computed and compared the 1D and 3D radiative
85 fluxes and heating rates by clouds. For example, Barker et al. [2011, 2012] and Okata et al. [2017]
86 compared the 1D and 3D SW fluxes computed based on the constructed A-Train cloud scenes at the TOA
87 and surface. A more recent study by Singer et al. [2021] utilized Large-Eddy Simulations (LES) cloud fields
88 of different cloud regimes to assess the SW radiative flux and TOA albedo bias associated with the 3D
89 effects. The main difference between their study and this current work is as follows: They compared the
90 3D (i.e., Box F in **Fig. 1**) with the 1D broadband fluxes (i.e., Box G in **Fig. 1**) both computed from the “true”
91 clouds. In contrast, we argue that the “true” clouds are not known in practice and therefore we compare
92 the 3D flux (i.e., Box F in **Fig. 1**) with the 1D flux computed from the “retrieved cloud properties” (i.e., Box
93 E in **Fig. 1**), this approach enables us to measure the impact of cloud retrieval errors on the radiative flux
94 and CRE.



95
96 **Fig. 1.** Conceptual framework to understand the study. R_{3D} and R_{1D} are the reflectance from three dimensional (3D) and one
97 dimensional (1D) radiative transfer (RT) respectively, while δR is their difference. X represent the true cloud field and $X^*(R_{3D})$

98 is the retrieved cloud properties from 3D RT reflectance, while δX is the cloud property retrieval bias. F_{1D}^* and F_{1D} are the
99 radiative flux calculated using 1D RT on the retrieved cloud properties and true cloud properties respectively. F_{3D} is the radiative
100 flux derived from the true cloud field using 3D RT. δF_1 and δF_2 are the difference between the pair (F_{1D}^*, F_{3D}) and (F_{1D}, F_{3D}) ,
101 respectively.

102 To determine whether biased cloud retrievals of cloud properties can still provide an observational basis
103 for CRE, we focus on three important scientific questions (SQs) as illustrated in **Fig. 1**:

- 104 • SQ 1: How does the reflectance simulated based on 3D RT (R_{3D}) compare with the reflectance
105 simulated based on 1D RT (R_{1D}) for different types of clouds at different illuminating-viewing
106 geometries? (i.e., Comparing Box C to B in **Fig. 1**).
- 107 • SQ 2: How does the “retrieved cloud properties”, e.g., cloud optical thickness and cloud droplet
108 effective radius derived from the 3D reflectance using 1D RT, compare to the “true” cloud
109 properties? (i.e., Comparing Box D to A in **Fig. 1**).
- 110 • SQ 3: Comparing δF_1 to δF_2 in **Fig. 1**: i.e., how are the broadband SW radiative fluxes derived
111 from the retrieved cloud properties using 1D RT, F_{1D}^* (see Box E in **Fig. 1**) different from the “true”
112 radiative fluxes computed from the “true” cloud fields using 3D RT, F_{3D} (see Box F in **Fig. 1**) ? And
113 how does this result compare with the difference between F_{3D} and the broadband SW radiative
114 fluxes computed from the “true” cloud properties using 1D RT, F_{1D} (see Box G in **Fig. 1**).

115 The paper’s remaining structure is arranged as follows: Section 2 briefly describes the data and theory for
116 the study. Section 3 presents and discusses results on how the 3D radiative effects influences the radiance
117 fields, cloud property retrievals and broadband radiative flux. The summary and conclusion are given in
118 Sect. 4.

119 2. Data and Theory

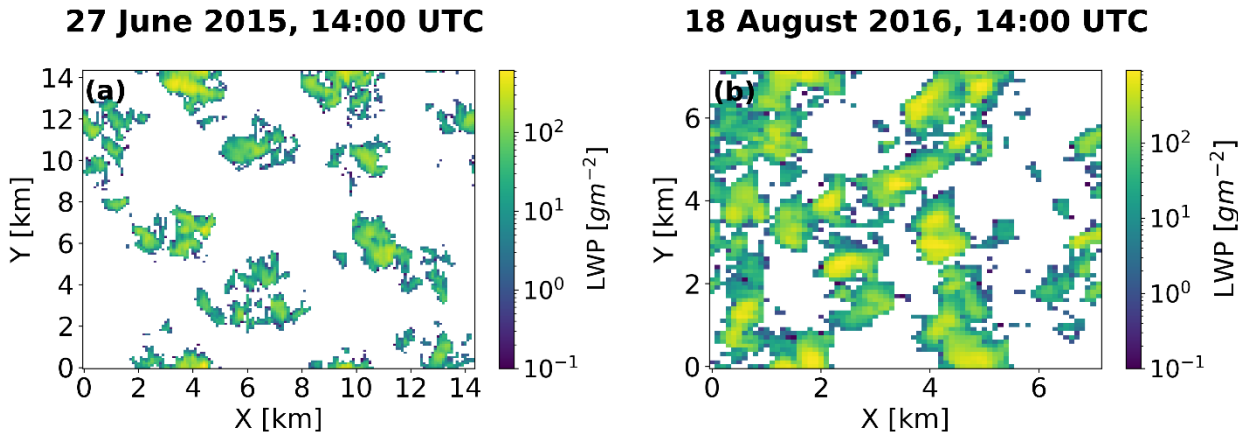
120 2.1. Cloud field data set

121 A great challenge facing 3D radiative effects studies is that the “true” clouds are always obscured by
122 the 3D radiative effects which are inevitable in real observations. To overcome this challenge, many
123 previous studies [e.g., Zhang et al., 2012; Miller et al., 2018; Rajapakshe and Zhang, 2020] have used
124 synthetic cloud fields and RT simulations to mimic the observation-retrieval process and study the 3D
125 radiative effects. Building on these previous studies, we adopt the same state-of-the-art satellite retrieval
126 simulator by Zhang et al. [2012] and added a broadband flux computation function to study the 3D
127 radiative effects and its impact on broadband SW radiative flux. As described in Zhang et al. [2012] and
128 illustrated in **Fig. 1**, the framework consists of three major components: 1) Synthetic cloud fields; 2) RT
129 models (for radiance and broadband flux simulations); 3) cloud property (e.g., τ and r_e) retrieval
130 simulator. LES cloud fields which are commonly used in different cloud microphysical and 3D effects studies
131 [e.g., Singer et al., 2020, Zhang et al., 2012] are based on computational models and mathematical
132 equations to simulate the atmospheric behavior and get the 3D cloud property, certain studies [e.g., Levis
133 et al., 2015; Loveridge et al., 2023] have developed atmospheric tomography techniques to reconstruct 3D
134 cloud scenes from observational data but are yet to be widely used globally. Similar to Zhang et al. [2012],
135 the synthetic cloud fields utilized in this study are based on LES cloud fields.

136 Since the 3D radiative effects on overcast clouds are minimal, two cloud fields of low and
137 intermediate cloud fractions have been selected as a case study to illustrate the framework explained in
138 Sect. 1. The selected cloud fields were from the LES Atmospheric Radiation Measurement (ARM)

139 Symbiotic Simulation and Observation (LASSO) Activity, conducted in the ARM Southern Great Plain (SGP)
 140 site located in Lamont, Oklahoma [Gustafson et al., 2020]
 141 (<https://www.arm.gov/capabilities/modeling/lasso/>). LASSO enhances ARM’s observations by using LES
 142 modeling to provide contextual and self-consistent representation of the atmosphere surrounding the
 143 ARM site. It also provides continuous observations from ground-based cloud and radiometric instruments
 144 which is valuable for enhancing research on cloud-radiation interactions. For this study, the two snapshots
 145 of LASSO LES cloud field cases analyzed are: 14:00 UTC on 27 June 2015, simulation ID=108 [ARM user
 146 facility, 2015] and the other at 14:00 UTC on 18 August 2016, simulation ID=113 [ARM user facility, 2016].
 147 For conciseness in this text, these snapshots will be referred to as “27 June” and “18 August” respectively.
 148 We chose to use these specific LASSO LES cloud fields data from the stated dates, because it represents
 149 typical shallow cumulus clouds, does not contain ice (to avoid the complexities dealing with ice
 150 microphysics) and has better diagnostic statistics compared to other LES data streams. It is important to
 151 note that, because the impact of 3D radiative effects vary substantially for different cloud regimes and
 152 surface types, this study is constrained to shallow cumulus cloud types (over land surface) found in the
 153 LASSO SGP site.

154



155

156 **Fig. 2.** Large-Eddy Simulation (LES) of cloud liquid water path (LWP) for 14:00 UTC, 27 June 2015 (a), and 14:00 UTC, 18 August
 157 2016 (b) at the ARM SGP atmospheric observatory. White areas are clear-sky regions where cloud liquid water path (LWP) =0.

158 The LASSO LES cloud fields for this study are characterized by broken cloud patterns spatially
 159 distributed across the domain as seen in the LWP maps in **Fig. 2a and b** for the 27 June and 18 August
 160 cases, respectively. The 3D distribution of cloud liquid water content (LWC) was obtained from the LASSO
 161 cloud fields data and a two-moment bulk microphysics scheme by Morrison and Gettelman [2008] (see
 162 their equation 5 in Sect. 2) was used to obtain the r_e associated with the corresponding LWC distribution.
 163 It is important to note that for this study, a cloudy column has been defined as a column with $LWP > 0$
 164 (i.e., clear-sky regions have $LWP=0$). The cloud fields have different domain sizes and microphysics
 165 distribution, and the cloud cover for the 18 August cloud field (47.08%) is more than twice that of the 27
 166 June cloud field (20.15%). Information about the cloud properties and the LES domain are summarized in
 167 **Table 1.**

168 **Table 1.** Cloud property characteristics for the LES cloud field cases. The mean cloud effective radius (r_e), mean cloud optical
 169 thickness (τ), and In-cloud liquid water path are from the average of the cloudy regions only. The columns from left to right are

170 case name, cloud fraction, mean In-cloud liquid water path, mean cloud base height (CBH), mean cloud top height (CTH), mean
 171 r_e , mean τ , grid spacing, and domain size, respectively.

Case name	CF (%)	Mean In-cloud LWP (gm^{-2})	Mean CBH (km)	Mean CTH (km)	Mean r_e (μm)	Mean τ	Grid spacing (m)	Domain size (km^3)
27 June 2015, 14:00 UTC	20.15	51.08	1.979	2.173	7.196	10.95	$\Delta x = \Delta y = 100, \Delta z = 30$	14.4x14.4x ~2.8
18 August 2016, 14:00 UTC	47.08	127.67	1.2691	1.6040	8.020	23.24	$\Delta x = \Delta y = 100, \Delta z = 30$	7.2 x 7.2 x ~2.4

172
 173 **2.2. Radiative Transfer Setup**

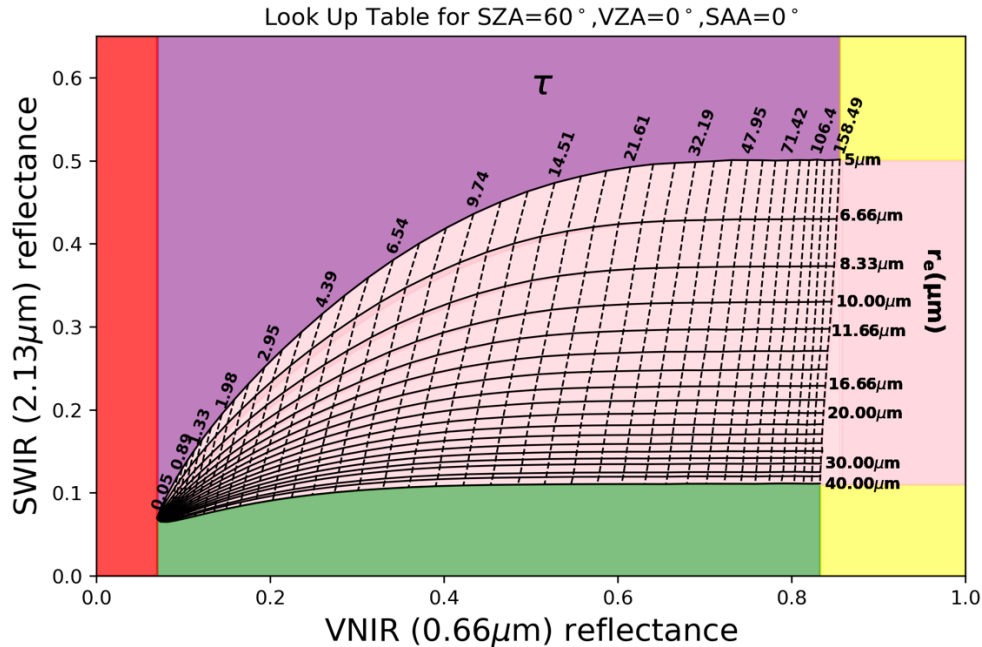
174 We use the spherical harmonics discrete ordinate method (SHDOM) RT model developed by Evans
 175 [Evans, 1998] to handle both 1D and 3D radiance computations. We have benchmarked the SHDOM
 176 simulations against the results from our previous studies [Zhang et al., 2012; Miller et al., 2016].
 177 Broadband SW radiative flux computations, both 1D and 3D, were performed with the Intercomparison
 178 of 3D Radiation Codes (I3RC) Monte Carlo community model [Pincus and Evans, 2009], and atmospheric
 179 gaseous absorption was incorporated via the SW Rapid Radiative Transfer Model (RRTM) correlated
 180 k-distribution approach [Mlawer et al., 1997] which consists of 14 bands with spectral range from 0.2 to
 181 12 μm (This coupled broadband radiative flux solver is hereafter known as the “I3RC+CKD” model).
 182 Rayleigh scattering was included in the flux RT calculations, the background atmospheric profiles are taken
 183 to be horizontally homogeneous throughout the domain and the profiles of atmospheric temperature,
 184 pressure, ozone, air density and water vapor utilized for the RT flux calculations were obtained from the
 185 sounding data at the ARM SGP site on 27 June 2015. Several studies [e.g., Gristey et al., 2022] have shown
 186 that aerosol embedded in clouds with small aspect ratios (similar to our chosen LASSO LES cloud fields)
 187 have significant influence on the 3D radiative effect. Thus, for simplicity in our study, ambient aerosols
 188 are neglected in the RT calculations. The 1D broadband RT flux calculations were performed with the same
 189 I3RC+CKD model, by dividing the LES domain into individual columns and RT was calculated on each LES
 190 column properties separately and independently.

191 The spectral cloud optical properties were calculated using Mie scattering theory and were
 192 averaged over each of the RRTM spectral bands. The phase functions were represented using Legendre
 193 coefficients with 35 log spaced effective radius spanning from 2 to 40 μm . The surface was assumed to be
 194 Lambertian with surface spectral albedos obtained from the ARM SGP site [see figure 4 in Coddington et
 195 al., 2013] applied for wavelength (λ) in the range $0.2 \leq \lambda \leq 2.5 \mu\text{m}$, while surface spectral albedo
 196 corresponding to a vegetative covered surface [Zhuravleva et al., 2009] was utilized for $\lambda > 2.5 \mu\text{m}$ (see
 197 Appendix for surface spectral albedo plot used in this study). In the Monte Carlo calculations, 10^8 and 10^4
 198 photons were initiated for calculations of the 3D broadband SW flux and the column-independent 1D
 199 broadband SW flux, respectively. The radiative transfer calculations were implemented for two solar
 200 zenith angles (SZAs), a high sun case with SZA of 5° and a low sun case with SZA of 60° . In the broadband
 201 flux calculations, the downward flux at the top of the domain (TOD) corresponds to 1363 Wm^{-2} and 684.1
 202 Wm^{-2} for SZA 5° and 60° , respectively. Throughout this study, we choose a constant 0° solar azimuth

203 angle (SAA) and a constant 0° viewing zenith angle (VZA). Double periodic horizontal boundary conditions
 204 were applied for all the RT calculations, and all RT calculations have been conducted at the native LES
 205 resolution of 100 m. Current satellite remote-sensing instruments have different footprints (e.g., 1 km
 206 footprint for MODIS instrument), which can have different 3D effects signatures on the retrievals and
 207 impact the derived radiative flux. Therefore, future studies will investigate how 3D effects retrieval errors
 208 for different spatial resolutions (coarse and fine) affect the radiative flux estimates.

209 **2.3. Bi-spectral retrieval method**

210 The bi-spectral retrieval method introduced in Sect. 1, is solely based on the 1D RT theory to interpret the
 211 observed cloud reflectance. It is implemented using a precomputed Look up table (LUT) which consists of
 212 1D reflectance function for different τ and r_e combinations at the required solar-view geometry (an
 213 example LUT is shown in **Fig. 3**). The observed cloud reflectance is then utilized as inputs to the LUT to
 214 simultaneously retrieve the τ and r_e via a two-dimensional (2D) interpolation between the observed
 215 cloud reflectance and the LUT grid. Notably, in the bi-spectral LUT regions with smaller τ , the retrieval
 216 uncertainty increases because the isolines of the LUT τ are less orthogonal and more tightly packed.



217
 218 **Fig. 3.** An example Nakajima and King bi-spectral Look up table (LUT) space. The solid lines are the reflectance function
 219 contours for fixed cloud effective radius (r_e), while the dashed lines are for fixed cloud optical thickness (τ). Surface is
 220 Lambertian with surface albedo=0.07. The solar zenith angle (SZA) is 60° , the view zenith angle (VZA) is 0° , and the solar
 221 azimuth angle (SAA) is 0° .

222 This non-linearity in the LUT has high inhomogeneity consequences for cloud retrievals at the pixel level
 223 [Zhang et al., 2012, 2016]. In this study, the VNIR reflectance were measured at $0.66 \mu\text{m}$ (identical to the
 224 central wavelength of operational MODIS retrieval algorithm over a vegetative land surface), while the
 225 SWIR reflectance were measured at the $2.13 \mu\text{m}$ wavelength. The LUT utilized for our bi-spectral retrievals
 226 have 19 effective radii spanning from 5 to $40 \mu\text{m}$, and 43 log spaced τ values spanning from 0.05 to 158.48.
 227 While a constant effective variance (v_e) value of 0.1 is used for consistency with all other RT simulations

228 in this study. The surface albedo in both 0.66 and 2.13 μm wavelengths for the LES radiance simulations
229 and LUT RT calculations was 0.07. This value is consistent with the surface albedo of similar spectral bands
230 in the broadband SW flux computations (see spectral albedo plot in Appendix).

231

232 **2.4. Classification of failed and successful retrievals**

233 One major challenge in cloud property retrievals from satellite remote sensing instruments like
234 MODIS, is the so called “failed retrievals”. A retrieval can be considered failed if there is no r_e and τ LUT
235 grid combination to interpret the reflectance observation, or if there is no realistic cloud microphysics to
236 explain the retrieved cloud property (e.g., a retrieved $r_e > 40 \mu\text{m}$). These can be due to several factors,
237 such as the limits of the LUT, clouds overlapping effect, presence of partially cloudy pixels, extreme solar-
238 satellite viewing geometries, strategy used in cloud mask implementation and the optical characteristics
239 of the underlying surface. Potential causes and rate of occurrence of failed MODIS retrievals for marine
240 liquid phase clouds have been studied extensively [Cho et al., 2015]. In this study, we refer to MODIS cloud
241 property retrieval algorithm’s classification of failed retrievals [Platnick et al., 2016] and the study by Cho
242 et al. [2015], to classify a pixel as successful or failed retrieval as explained below:

- 243 1) For observations with both VNIR and SWIR reflectance observations within the LUT solution
244 space, the nearest interpolated τ and r_e values are retrieved (Pink area bounded by the LUT lines
245 in **Fig. 3**). If the observed VNIR reflectance exceed the upper limit of LUT τ but within the LUT r_e
246 solution range (extended pink area in **Fig. 3**), the nearest LUT r_e is retrieved and the maximum
247 LUT τ value ($\tau=158.48$) is assigned to the retrieval. These explained categories are classified as
248 “successful retrievals” for this study.
- 249 2) In other cases, for observations with VNIR reflectance within the LUT solution space but SWIR
250 reflectance above the LUT solution space (purple area in **Fig. 3**), the nearest τ values are retrieved
251 but the smallest LUT r_e value of $5 \mu\text{m}$ is assigned to the retrievals. This category of retrieval failure
252 is called “ r_e too small” failures. In cases where the VNIR reflectance observations are within the
253 LUT τ solution space, but the SWIR reflectance are below the LUT solution space (green area in
254 **Fig. 3**) the nearest τ values are retrieved but the largest LUT r_e value of $40 \mu\text{m}$ is assigned to the
255 retrieval. This category of retrieval failure is called the “ r_e too large” failures. In cases where the
256 observed VNIR reflectance is greater than the largest LUT τ value and the observed SWIR
257 reflectance is smaller than the largest LUT r_e (i.e., the lower yellow region in **Fig. 3**), the retrievals
258 are assigned the largest τ value ($\tau=158.48$) and the largest r_e value ($r_e=40 \mu\text{m}$). For observations
259 with VNIR reflectance greater than the largest LUT τ value and the SWIR reflectance greater than
260 the smallest LUT r_e value (i.e., the upper yellow region in **Fig. 3**), the retrievals are assigned the
261 largest τ value ($\tau=158.48$) and smallest r_e value ($r_e=5 \mu\text{m}$). Lastly, for observations with VNIR
262 reflectance below the minimum LUT τ (red area in **Fig. 3**), the r_e and τ retrievals are assigned fill
263 values (which are represented by $\tau = 0$ in our flux calculations). These explained categories are
264 called “ τ ” failures. The r_e too small, r_e too large and τ failure categories are collectively classified
265 as “failed retrievals” for this study.

266

267 **2.5. Approach for radiative transfer simulation and result comparisons**

268 To address the three SQs for our study (identified in Sect. 1), we performed a total of fourteen
269 experiments for each cloud field. The first four experiments were performed with the SHDOM model to

270 study the 3D radiative effects on the observed reflectance and address SQ 1. It involves simulating and
 271 comparing R_{3D} with R_{1D} for the high and low sun cases. The next four experiments involve comparing
 272 cloud properties retrieved from R_{3D} (Box D in **Fig. 1**) and cloud properties retrieved from R_{1D} (Box B to A
 273 in **Fig. 1**) for both high and low sun, to examine the influence of the 3D radiative effects on the retrieved
 274 cloud properties and address SQ 2. These experiments were conducted using the 3D and 1D RT based
 275 reflectance as inputs to the precomputed LUT described in Sect. 2.3. The last six experiments were
 276 conducted with the I3RC+CKD to examine the impact of the 3D radiative effects on the broadband solar
 277 radiative flux for both high and low sun scenarios in the LES domains and address SQ 3. These experiments
 278 involve calculating for each SZA, F_{1D}^* from the retrieved cloud properties using 1D RT as well as computing
 279 F_{3D} and F_{1D} from the true cloud fields using 3D and 1D RT respectively. It is important to note that in the
 280 F_{1D}^* calculations, the retrieved cloud properties ($\tau^*(R_{3D})$ and $r_e^*(R_{3D})$) are utilized to calculate the
 281 retrieved LWP (using retrieved LWP $\cong 2\tau^*\rho r_e^*/3$, where ρ is the density of liquid water; [Stephens,
 282 1977; Liou, 1992]) which are then reconstructed into cloud effective radius and LWC distribution for each
 283 LES column while preserving the vertical structure of the original LES cloud field. 1D RT are then performed
 284 using the reconstructed retrieved clouds as inputs to obtain F_{1D}^* . Note, unless otherwise stated, for this
 285 study, the successful and failed retrievals (as described in Sect. 2.4) have been used to represent the total
 286 population of cloudy pixels in the cloud property inputs used to calculate F_{1D}^* . The calculation of F_{1D} is
 287 identical to that of F_{3D} except for the absence of the horizontal movement of photons between the LES
 288 grid columns. This enables us to determine the impact of neglecting the horizontal movement of photons
 289 on the broadband radiative fluxes. On the other hand, in reference to the F_{3D} , computing F_{1D}^* will not
 290 only help us to better understand the implications of neglecting the horizontal transport of photons but
 291 will also enable us to measure how biases in the retrieved cloud properties (which are affected by the 3D
 292 radiative effects) impact the broadband radiative fluxes.

293 In order to describe the impact of the 3D radiative effects on the radiance fields, retrieved cloud
 294 properties and broadband radiative flux, we first examine their effects across the LES domain and
 295 subsequently quantify their overall impact on the domain by computing the horizontally domain-averaged
 296 results and determine the absolute bias, hereafter referred to as “bias” for brevity and is defined as $\bar{y} - \bar{x}$
 297 , where \bar{y} denotes the domain-averaged result from the 3D RT quantity (e.g., Reflectance or flux), and \bar{x}
 298 denotes the domain-averaged result from the 1D RT quantity (e.g., Reflectance or flux).

299 To quantify the difference between the CRE computed from the benchmark F_{3D} and the CRE
 300 computed from F_{1D} or F_{1D}^* , we define a domain-scale quantity known as the relative cloud radiative
 301 effects (rCRE) bias as:

$$302 \quad \text{rCRE bias} = \left(1 - \frac{\text{CRE}_{1D}}{\text{CRE}_{3D}}\right) \times 100 \quad (1)$$

303 Where CRE_{1D} is the CRE calculated from either F_{1D} or F_{1D}^* in units of Wm^{-2} and CRE_{3D} is the CRE
 304 calculated from F_{3D} in units of Wm^{-2} . According to this definition, a rCRE bias of 0% would indicate that
 305 there is no bias between the CRE computed from F_{1D} or F_{1D}^* and the CRE computed from F_{3D} . This, imply
 306 that the CRE computed from F_{1D} or F_{1D}^* is equivalent to the CRE computed from F_{3D} . A positive rCRE bias
 307 greater than 0% would quantify the percentage by which the CRE computed from F_{1D} or F_{1D}^* is lesser than
 308 the CRE computed from F_{3D} , and thus indicate that the 1D calculations (F_{1D} , F_{1D}^*) underestimate the CRE
 309 relative to F_{3D} . Also, a negative rCRE bias less than 0% would quantify the percentage by which the CRE
 310 computed from F_{1D} or F_{1D}^* exceeds the CRE computed from F_{3D} and imply that the calculations from
 311 F_{1D} or F_{1D}^* overestimate the CRE relative to F_{3D} .

312 3. Results and discussion

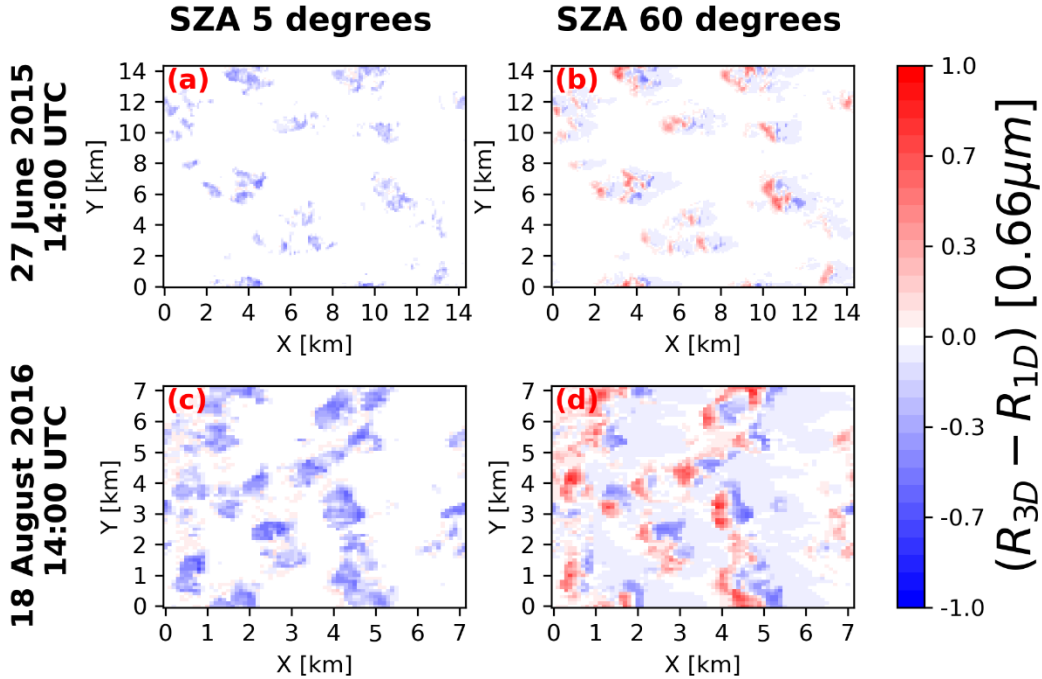
313 3.1. Investigating the 3D radiative effects on simulated reflectance

314 Focusing first on SQ 1, we compare R_{1D} and R_{3D} to assess the impact of the 3D radiative effects on
315 the reflectance radiation field, i.e., Box B vs. Box C in the framework of **Fig. 1**. Specifically, we will
316 investigate the reflectance bias, δR ($\delta R = R_{3D} - R_{1D}$) at the two λ (0.66 and 2.13 μm) required for our
317 bi-spectral retrieval for both low sun (SZA 60°) and high sun (SZA 5°) cases. To describe the 3D radiative
318 effects on the observed reflectance, classifications are made based on the increase in the brightness of a
319 pixel in the LES domain. A pixel in the LES domain is considered “brightened” (“darkened”) if its 3D
320 RT-based reflectance is higher (lower) than its 1D counterpart.

321 Maps of δR at $\lambda = 0.66 \mu\text{m}$ ($\delta R_{\lambda=0.66\mu\text{m}}$) for the two cloud fields when the sun is high and low are
322 shown in **Fig. 4**. In the low sun case, the deviation of the 1D RT-based simulated reflectance from the 3D
323 RT-based simulated reflectance leads to δR with distinct pattern of brightening and darkening observed
324 in some pixels across the LES domain. A closer examination of $\delta R_{\lambda=0.66\mu\text{m}}$ within cloudy regions in the
325 low sun case for the two cloud fields (**Fig. 4b,c**) reveals a consistent pattern; the brightened pixels, where
326 $\delta R_{\lambda=0.66\mu\text{m}}$ is positive, are predominantly observed in sunlit regions that directly face the sun located on
327 the left (e.g., at X=3.5 km, Y=14 km in **Fig. 4b**). On the other hand, darkened pixels, where $\delta R_{\lambda=0.66\mu\text{m}}$ is
328 negative, are observed on the opposite side of the cloud layer (e.g., at X=5 km, Y=14 km in **Fig. 4b**). These
329 findings are consistent with previous 3D radiative effects studies for oblique solar geometry [e.g., Várnai
330 and Davies, 1999; Várnai, 2000; Marshak et al., 2006]. The observed opposing effects of brightening and
331 darkening in the low sun angle case does not only depend on the orientation of the cloud towards or away
332 from the sun, other factors like cloud-cloud interactions, cloud geometry and aspect ratio, spatial
333 distribution of the cloud in the domain and the horizontal transport of photons also contribute to these
334 behaviors [Várnai and Marshak, 2001, 2002; Marshak and Davis, 2005; Marshak et al., 2006; Zhang et al.,
335 2012].

336 In the case of the high sun, the sun is almost perpendicular (at SZA 5°), and its radiation interaction with
337 clouds under 3D RT is different from that of the low sun case. In 3D RT at high sun, the original direction
338 of photons is downwards (due to the sun’s small angle of inclination to the vertical) and on striking a cloud,
339 some photons are scattered and some leak from optically thick to optically thin cloudy regions and even
340 out of cloud sides [O’Hirok and Gautier, 1998] down to the surface where they are absorbed. This is
341 because for photons trajectories with low number of scattering trajectories and high sun, photons leaking
342 out of cloud sides are statistically more likely to continue moving downwards towards the surface where
343 they are absorbed. These leaking of photons to surrounding clouds and the surface results in net photon
344 loss in the thick cloud regions, which explains the darkening of the thick clouds and brightening of the
345 surrounding thin clouds compared to 1D RT results. Hence, $\delta R_{\lambda=0.66\mu\text{m}}$ is mainly negative across the LES
346 domain for the high sun (**Fig. 4a,c**). The darkening characteristics is more pronounced in the 18 August
347 case because it consists of a larger distribution of thicker clouds compared to the 27 June cloud field; large
348 number of photons leaking from optically thicker clouds results in more significant reduction in the
349 reflectance values and more prominent darkening effect than photons leaking from optically thinner
350 clouds. Similar reflectance characteristics are observed for the 2.13 μm band (not shown).

351



352

353 **Fig. 4.** Maps of the reflectance bias ($\delta R = R_{3D} - R_{1D}$) for wavelength $0.66 \mu\text{m}$ at Solar zenith angle (SZA) 5° (a) and (c) for the
 354 27 June and 18 August cases respectively and SZA 60° (b) and (d) for the 27 June and 18 August cases respectively. The direction
 355 of view is at nadir. For SZA 5° , the sun is almost perpendicular to the domain but slightly tilted to the left. For SZA 60° the sun is
 356 on the left of the domain.

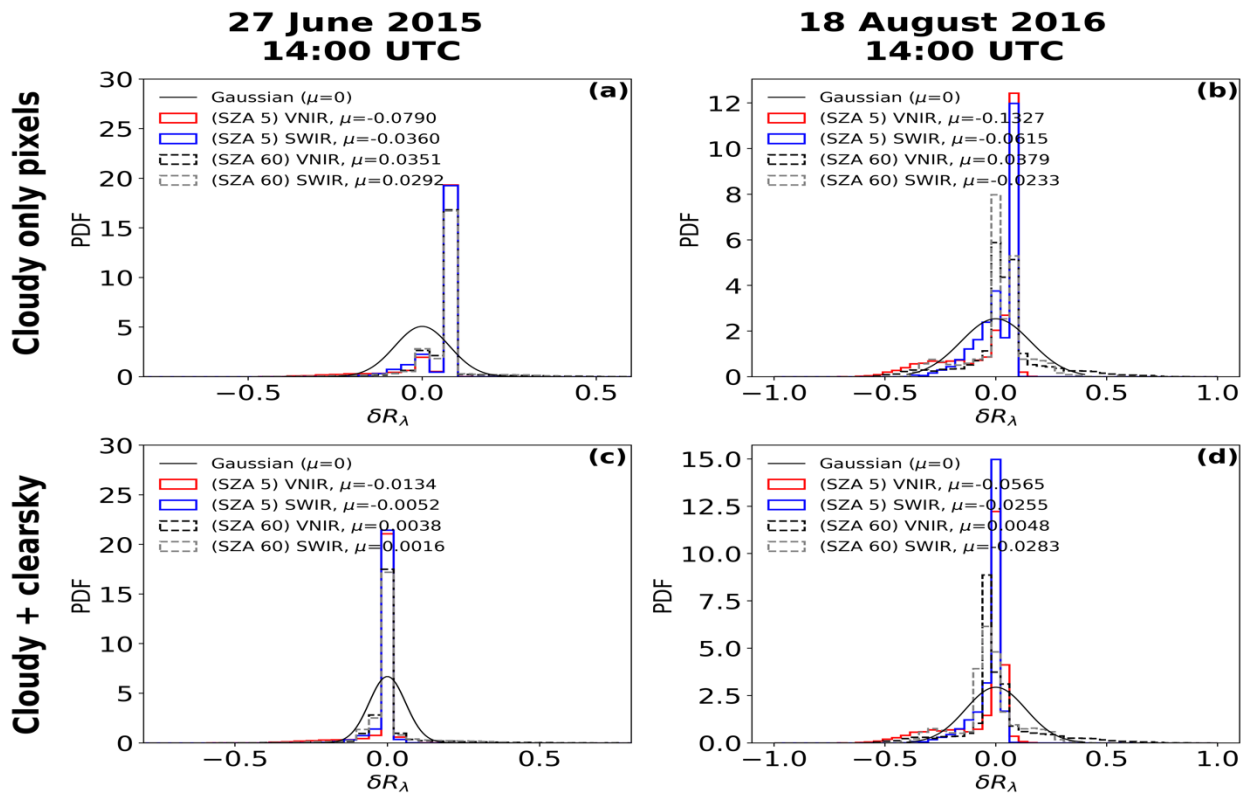
357 To examine the statistical characteristics of δR in the LES domain, the probability density function
 358 (PDF) of δR for “cloudy only” pixels are analyzed to investigate the 3D radiative effects on the observed
 359 cloud reflectance. Subsequently, we compared this PDF to δR for both “cloudy and clear-sky” pixels (i.e.,
 360 the whole LES domain) to highlight the effects of cloud presence on the overall reflectance bias within the
 361 LES domain.

362 The PDFs of δR for cloudy only pixels in the low sun case (broken black and gray lines in **Fig. 5a**,
 363 **b**) are characterized by positive and negative distribution in both VNIR and SWIR bands (corroborating the
 364 brightening and darkening effects in Error! Reference source not found.**b,d**). The overall positive δR
 365 observed in the VNIR and SWIR bands (domain mean δR of 0.0351 (0.0292) for the VNIR (SWIR) band in
 366 the 27 June case and 0.0379 for the VNIR band in the 18 August case) indicates that the brightening effects
 367 is predominant when only cloudy pixels are considered. Meanwhile, δR is -0.0233 for the SWIR band in
 368 the 18 August case. This negative δR is due to a high net loss of photons in 3D RT reflectance (more
 369 photons leak from clouds to the surface where they are absorbed, than those reflected from clouds)
 370 compared to the 1D RT results. On the other hand, the PDFs of δR for the cloudy and clear-sky pixels
 371 (broken black and gray lines in **Fig. 5c, d**) is almost similar to that of the cloudy only but shows a shift of
 372 the distribution leftwards, almost centered around zero. This is expected because clear-sky regions not in
 373 the vicinity of any clouds exhibit negligible 3D radiative effects, which causes the distribution to shift closer
 374 to zero, since the cloud fraction for both cloud cases is less than 50%. The horizontal movement of photons
 375 from cloudy to surrounding clear-sky regions increase the 3D reflectance of clear-sky areas around the
 376 sunlit cloudy regions but the strong darkening effects on the clear-sky regions located opposite the sunlit
 377 direction dominates the clear-sky only areas, and results in a negative mean bias when the reflectance of

378 clear-sky only pixels are examined. Interestingly, the mean δR for the cloudy and clear-sky pixels are of
 379 the same sign with the cloudy only values, which indicates that the cloudy pixels have significant effect on
 380 the domain-scale statistics.

381 The PDFs of δR in the case of the high sun for cloudy only pixels show a larger distribution of pixels
 382 with positive δR in both the VNIR and SWIR band accompanied by longer tails to the left (red and blue
 383 solid lines in **Fig. 5a, b**). However, the δR for both cloud cases present negative values in the VNIR and
 384 SWIR bands. These observations suggest that large radiation/photos leak from a small number of thick
 385 cloud pixels to a larger number of thin clouds. This phenomenon therefore increases the number of
 386 thin clouds with positive reflectance bias, although of very small magnitude when compared to the
 387 negative biases.

388



389

390 Fig. 5. PDF (Probability density function) of reflectance bias (δR) for cloudy only pixels for the 27 June case (a) and 18 August case
 391 (b). PDF of reflectance bias for cloudy and clear-sky pixels for the 27 June case (c) and 18 August case (d). μ is the domain mean
 392 reflectance bias. A gaussian distribution (solid black curve) with standard deviation for the 0.66 μ m band at SZA 5 degrees and
 393 centered around zero is shown in all panels.

394 Similar to the low sun case, the PDF of δR when both cloudy and clear-sky pixels for the high sun
 395 case are considered (red and blue solid lines in **Fig. 5c, d**), shows a significant distribution of values close
 396 to zero. Due to the leaking of photons from thick clouds to thin clouds and clear-sky regions surrounding
 397 the clouds, there is an increase in the 3D reflectance of clear-sky regions. Additionally, when the sun is
 398 high at SZA of 5° , there are very minimal shadows cast on the clear-sky regions. These two highlighted
 399 reasons result in a positive δR for the clear-sky only region. Thus, the negative value of δR for the cloudy

400 and clear-sky (same sign as the cloudy only) indicates that the domain scale reflectance bias is dominated
 401 mainly by the cloudy only pixels and they play a significant role in the domain-scale statistics.

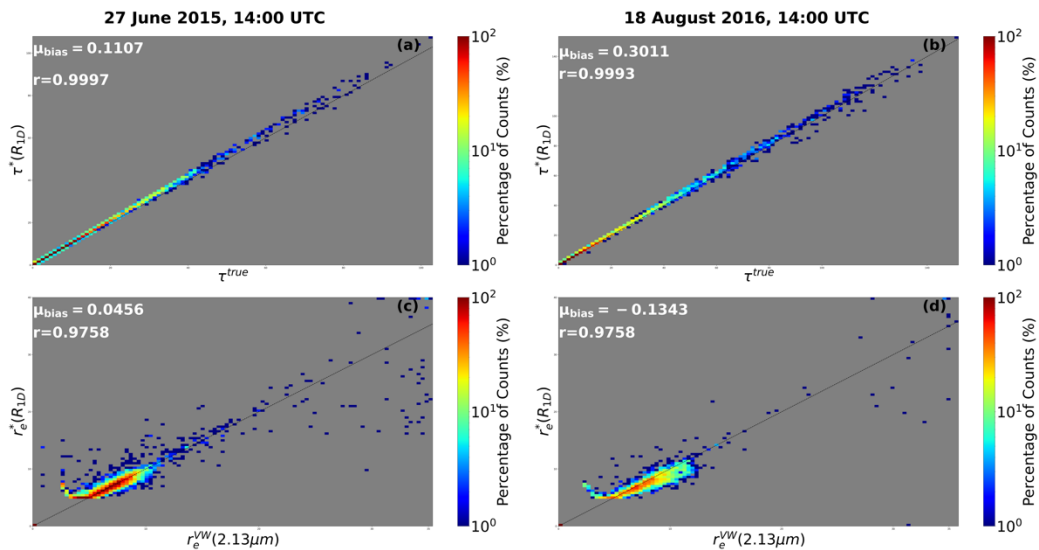
402

403 3.2. Investigating the 3D radiative effects on cloud retrievals

404 Focusing on SQ 2 in this section, we investigate how δR , as discussed in the previous section, affect
 405 r_e and τ retrievals (i.e., Box A vs. Box D in the framework of **Fig. 1**). We utilize R_{1D} as inputs for the LUT
 406 (explained in Sect. 2.3) to retrieve the 1D RT-based cloud droplet effective radius ($r_e^*(R_{1D})$) and cloud
 407 optical thickness ($\tau^*(R_{1D})$). Additionally, we use R_{3D} as inputs for the LUT to retrieve the 3D RT-based
 408 cloud droplet effective radius ($r_e^*(R_{3D})$) and cloud optical thickness ($\tau^*(R_{3D})$).

409 Before discussing analysis of the 3D and 1D RT-based retrievals comparison, we first check the accuracy
 410 of our retrievals by comparing the original LES cloud properties with our 1D RT-based retrievals (i.e.,
 411 comparing retrievals from 1D radiance in Box C with cloud properties in Box A in **Fig. 1**). For this purpose,
 412 the τ from the original LES (τ^{true}) is the vertical integration of the visible (0.66 μm) extinction coefficient
 413 of each column from cloud base to cloud top. For the LES r_e , we follow Zhang et al. [2017] analytical
 414 vertical weighting function (see their equation 4) to get the vertically weighted cloud droplet effective
 415 radius (r_e^{VW}) where the $\mu_o = 0.5$, $\mu=1$ and the vertically weighting function parameter (b) associated with
 416 the 2.13 μm band was set to 2 to allow for a deeper penetration depth and for better correlation between
 417 the r_e^{VW} (2.13 μm) and bi-spectral retrievals.

418 **Fig. 6** shows the comparison between the r_e^{VW} (2.13 μm) and the $r_e^*(R_{1D})$ as well as τ^{true} with the
 419 $\tau^*(R_{1D})$ for the two cloud fields at SZA=60° and VZA=0°. For this comparison, the mean τ and r_e biases
 420 are $\mu_{\tau bias} = \langle \tau^*(R_{1D}) - \tau^{true} \rangle$ and $\mu_{r_e bias} = \langle r_e^*(R_{1D}) - r_e^{VW}(2.13 \mu m) \rangle$



421

422 **Fig. 6.** Joint histogram of bi-spectral retrieved τ based on 1D RT simulated reflectance $\tau^*(R_{1D})$ vs Vertically integrated τ (τ^{true})
 423 for the 27 June case (a) 18 August case (b). Joint histogram of bi-spectral retrieved r_e based on 1D RT simulated reflectance
 424 ($r_e^*(R_{1D})$) vs. vertically weighted effective radius ($r_e^{VW}(2.13 \mu m)$) in (c) and (d) $\mu_{bias} = \langle retrieved\ cloud\ property -$
 425 $reference\ cloud\ property \rangle$.

426 For the two cloud fields considered in this study, the $\tau^*(R_{1D})$ is highly correlated with the τ^{true}
 427 as seen in the joint histogram plots (**Fig. 6a** and **b**) with a correlation coefficient (r) of 0.9997 for the 27
 428 June case, and a r of 0.9993 for the 18 August case, although both have a slight positive mean bias
 429 ($\mu_{\tau\ bias} = 0.1107$ and 0.3011 for the 27 June and 18 August cases respectively). Also, the comparisons of
 430 the $r_e^*(R_{1D})$ with the r_e^{VW} ($2.13\ \mu m$) in **Fig. 6c** and **d**, shows good correlation ($r > 0.96$) for both cloud
 431 cases, and slightly positive mean biases ($\mu_{r_e\ bias} = 0.0456$) for the 27 June case and a negative mean bias
 432 ($\mu_{r_e\ bias} = -0.1343$) for the 18 August case. Certain extreme outliers bias is observed in the r_e
 433 comparisons, these outliers are attributed to thin clouds and have been studied by Miller et al. [2018].
 434 Several studies [e.g., Miller et al., 2016, 2018; Zhang et al., 2012] have investigated the accuracy of 1D
 435 bi-spectral retrievals compared to vertically weighted retrievals as well as the impact of cloud vertical
 436 profile on bi-spectral retrievals. Since we have good agreement between retrievals from the 1D RT-based
 437 reflectance and the original LES cloud field properties, this study will use the $r_e^*(R_{1D})$ and $\tau^*(R_{1D})$ as the
 438 reference cloud properties and directly compare them with the $r_e^*(R_{3D})$ and $\tau^*(R_{3D})$ to investigate the
 439 impacts of 3D radiative effects on the retrievals.

440 In the high sun case retrievals, $r_e^*(R_{3D})$ are overestimated and $\tau^*(R_{3D})$ are underestimated
 441 compared to their 1D counterpart. This is because photons leaking from optically thick regions to optically
 442 thin cloudy regions and out of cloud sides down to the surface where they are absorbed, results in a net
 443 photon loss which make the 3D radiance field appear darker than its 1D counterpart (explained in Sect.
 444 3.1). Consequently, for retrievals, darkening shifts the reflectance observation on the LUT space leftwards
 445 and downwards to regions where the LUT r_e grid isolines represent larger droplet sizes and the LUT τ
 446 isolines represents thinner clouds. For the low sun case, $r_e^*(R_{3D})$ are underestimated and $\tau^*(R_{3D})$
 447 overestimated in brightened optically thick cloudy pixels (facing the sun) and $r_e^*(R_{3D})$ are overestimated
 448 and $\tau^*(R_{3D})$ underestimated in darkened pixels on its opposite cloud side. Larger $r_e^*(R_{3D})$ and smaller
 449 $\tau^*(R_{3D})$ compared to $\tau^*(R_{1D})$ and $r_e^*(R_{1D})$ in brightened pixels occurs since brightening phenomena in
 450 the LUT space shifts the observed reflectance upwards and rightwards where the LUT r_e grid isolines
 451 represents smaller droplets sizes and the LUT τ isolines represents thicker clouds. τ and r_e retrieval biases
 452 in satellite observations have been well documented in numerous studies [e.g., Várnai and Marshak, 2002;
 453 Zhang and Platnick, 2011; Zhang et al., 2012], and in common occurrence, overestimation of $\tau^*(R_{3D})$ is
 454 coupled with the underestimation of $r_e^*(R_{3D})$ and vice versa.

455 **Table 2** shows the frequency of failed and successful retrievals from R_{3D} for the two cloud fields
 456 considered in this study. It is observed that the number of failed retrievals is small for the SZA 5° case (<
 457 13%), while the retrieval failures are larger for the SZA 60° case (> 40%) for both cloud fields under
 458 consideration. The larger retrieval failures for the low sun case is mostly attributed to multiple scattering
 459 in the 3D RT due to increased path length (since original direction of travel of the photons from the sun is
 460 oblique), which increases radiation-cloud interaction and reflectance. Although, this leads mostly to τ
 461 failures, the other r_e type failures can arise from very darkened pixels (from photon leaking or cloud
 462 shadow) which shifts observation outside the LUT lower range (for r_e too large) or brightened pixels from
 463 less absorbing clouds which shifts the observations beyond the upper range of the LUT (for r_e too small)
 464 depending on the scenario.

465 **Table 2.** Statistics of successful and failed retrievals from the 3D RT-based radiance for the 27 June and 18 August cloud fields at
 466 Solar zenith angle (SZA) 5 and 60 degrees. The columns from left to right are Case name (Identified by date and time), solar zenith
 467

468 angle (SZA), Number of pixels with successful retrievals only, Pixels with failed retrievals, Total number of successful and failed
 469 retrievals.

Case name	SZA	No of pixels with successful retrievals only	Pixels with failed retrievals			Total number of successful and failed pixels
			Category of failed retrievals	No of pixels	Total	
27 June 2015, 14:00 UTC	5°	3670 (87.82%)	r_e too large	85 (2.03%)	509 (12.17%)	4179 (100%)
			r_e too small	365 (8.73%)		
			τ failures	63 (1.41%)		
	60°	2100 (50.16%)	r_e too large	97 (2.32%)	2079 (49.74%)	
			r_e too small	1035 (24.77%)		
			τ failures	947 (22.66%)		
18 August 2016, 14:00 UTC	5°	2344 (96.02%)	r_e too large	46 (1.88%)	97 (3.97%)	2441 (100%)
			r_e too small	29 (1.188%)		
			τ failures	22 (0.90%)		
	60°	1368 (56.04%)	r_e too large	339 (13.88%)	1073 (43.96%)	
			r_e too small	178 (7.29%)		
			τ failures	556 (22.77%)		

Values in parentheses are percentage of counts. (Percentage of counts = Number of affected pixels/ Total number of pixels)

470

471 3.3. Investigating the 3D radiative effects on the Broadband radiative flux

472

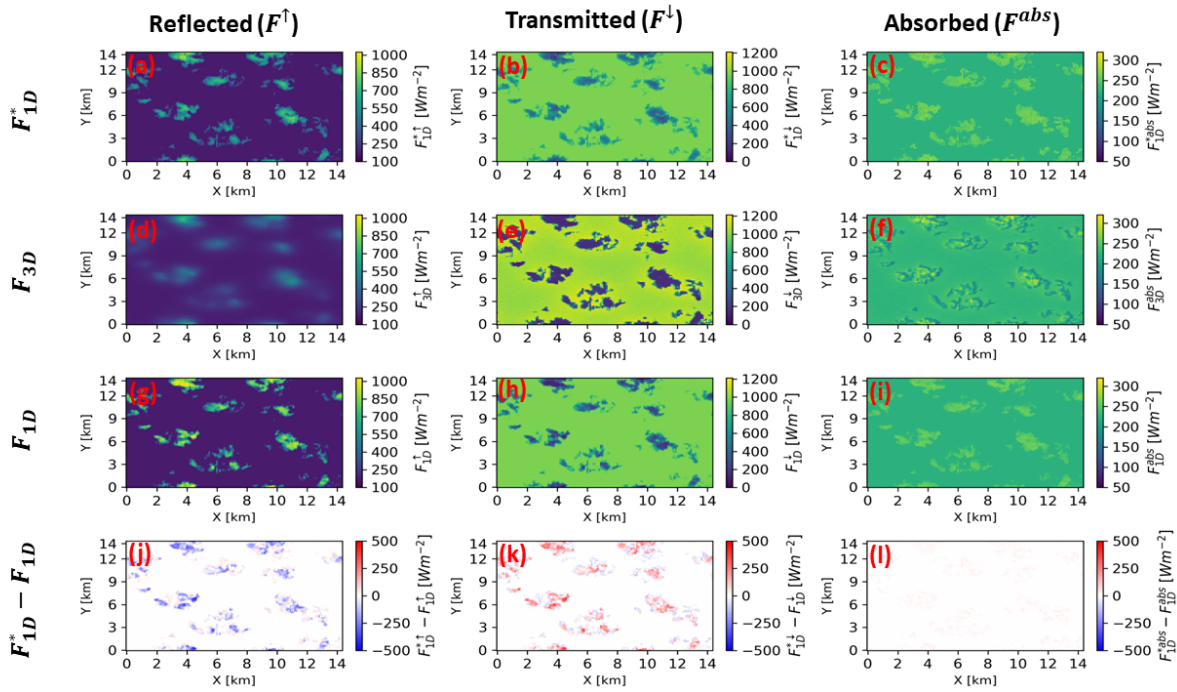
473 3.3.1. Investigating the 3D radiative effects on the broadband radiative flux: Using a 474 combination of the successful and failed retrievals as the input cloud property

475 Focusing on SQ 3 in this section, we will compare F_{3D} and F_{1D}^* to investigate the impact of cloud
 476 retrieval biases due to the 3D radiative effects on the broadband SW radiative flux. We will also compare
 477 F_{3D} and F_{1D}^* to study the impact of neglecting horizontal photons transport on the broadband SW flux
 478 results. Additionally, we compare δF_1 (i.e., $F_{3D} - F_{1D}^*$) with δF_2 (i.e., $F_{3D} - F_{1D}$) to determine errors in
 479 radiative flux estimates and evaluate the CRE.

480 It is important to note here that both the successful and the failed retrievals as described in Sect.
 481 2.4 are included in the RT simulations in the control simulations presented in this section. The motivation
 482 for including the failed retrievals is to preserve the impacts of this significant τ fraction of pixels on the
 483 domain averaged fluxes and CRE simulations, even though the retrieval of τ and r_e based on the bi-
 484 spectral method fails for them. In addition to the controlled simulations, we have also conducted
 485 sensitivity studies, where we exclude the failed retrievals in the analysis. The results are shown and
 486 discussed in the Appendix.

487 Maps of the simulated SW broadband radiative quantities (reflected flux at the TOD (F^\uparrow),
 488 transmitted flux at the surface (F^\downarrow), and column absorbed flux (F^{abs})) for the 27 June case at the high and
 489 low sun angles are presented in Fig. 7 and Fig. 8, respectively. These figures reveal several interesting and
 490 important points. First, it is interesting to note that the reflected flux in Fig. 7d seems blurry in comparison
 491 with 1D results in Fig. 7a and Fig. 7g. The same is also seen comparing Fig. 8d with Fig. 8a and Fig. 8g. This
 492 is because in 1D RT, simulation of the upwelling hemispheric flux at a given point at the TOD is determined
 493 only by the cloud and surface properties in the column beneath such point. In contrast, in 3D RT

494 simulation, it depends on the cloud and surface properties of both the corresponding column and a large
 495 extent of the surrounding columns, as a result of simple parallax effect. Therefore, the contrast between
 496 two adjacent columns in the 1D simulation, for example, a cloudy column and an adjacent clear-sky
 497 column next to it, is quite large, whereas the contrast for the same two columns in 3D simulation is much
 498 smaller because the two have a significant overlap in terms of the areas that have influences on their flux.
 499 Because of this fundamental difference between 1D and 3D simulations, a pixel-to-pixel comparison of
 500 the upwelling flux is not appropriate. Instead, we compare the domain-averaged statistics.

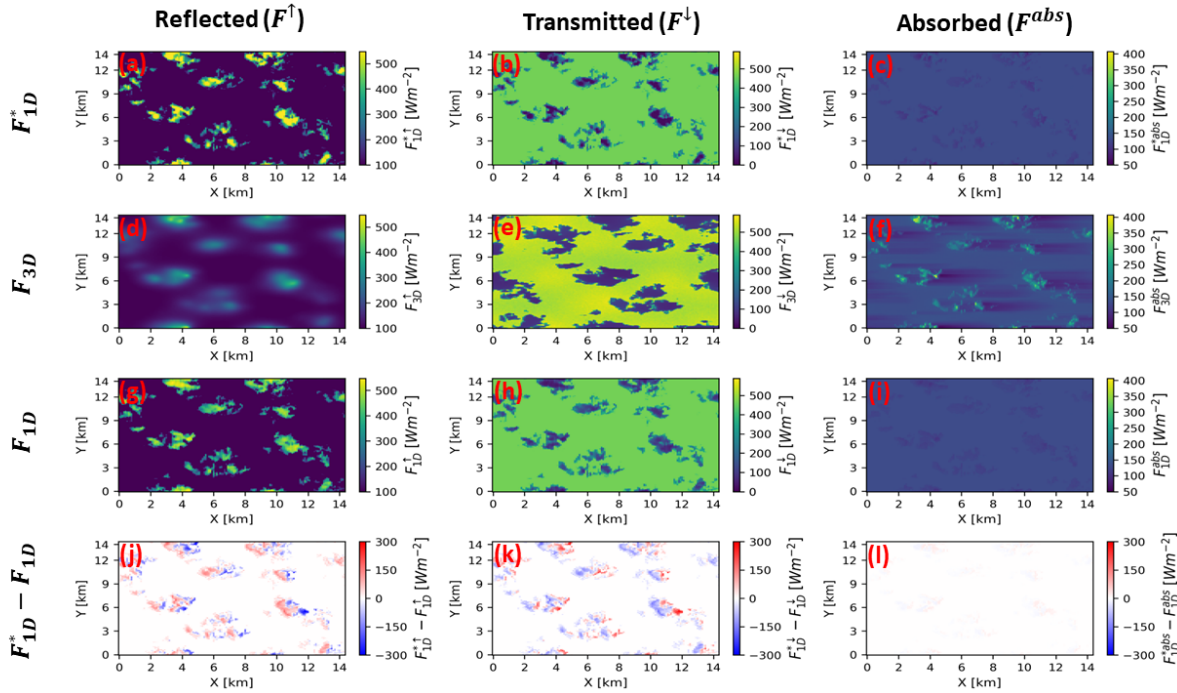


501
 502 **Fig. 7.** Simulated shortwave broadband Reflected flux at top of the domain (F^\uparrow), Transmitted flux at the surface (F^\downarrow) and Column
 503 absorbed flux (F^{abs}) derived from the retrieved clouds properties using 1D RT, F_{1D}^* (a)-(c), derived from the true clouds properties
 504 using 3D RT, F_{3D} (d)-(f), derived from the true clouds properties using 1D RT, F_{1D} (g)-(i) and difference between F_{1D}^* and F_{1D} (j)-
 505 (l) for Solar zenith angle= 5° and View zenith angle= 0° . Sun is high and slightly on the Left-hand side of the domain. The solar
 506 irradiance at the top of the domain scales with the cosine of the solar zenith angle.

507 Before we delve into that, we first aim to unravel how cloud property retrieval errors affect 1D RT flux
 508 solutions. For this purpose, we compare the F^\uparrow component of F_{1D}^* (denoted by $F_{1D}^{*\uparrow}$) with the F^\uparrow
 509 component of F_{1D} (denoted by F_{1D}^\uparrow). The same comparison is done between the F^\downarrow component of F_{1D}^*
 510 (denoted by $F_{1D}^{*\downarrow}$) and its counterpart from the F_{1D} (denoted by F_{1D}^\downarrow). The $F_{1D}^{*\uparrow}$ have visible signatures of
 511 the input cloud property retrievals. For instance, in the high sun case, smaller reflected flux values (recall,
 512 underestimated τ dominates retrievals from high sun radiance) dominate $F_{1D}^{*\uparrow}$ (**Fig. 7a**) as compared to
 513 F_{1D}^\uparrow (**Fig. 7g**). The underestimation of $F_{1D}^{*\uparrow}$ compared to F_{1D}^\uparrow is evident in **Fig. 7j**. This difference is also well
 514 captured in the domain-averaged values which will be discussed later in this section. In the low sun case,
 515 comparison between $F_{1D}^{*\uparrow}$ and corresponding F_{1D}^\uparrow reveals that in $F_{1D}^{*\uparrow}$, the overestimated retrieved τ areas
 516 characterized by thicker clouds (i.e., retrieved from brightened pixels) provides larger reflected flux values
 517 and the underestimated retrieved τ areas characterized by thinner clouds (i.e., retrieved from darkened
 518 pixels) have smaller reflected flux values than their F_{1D}^\uparrow counterpart (**Fig. 8j**). Their overall effect on the

519 domain reflected flux values depends on how the opposite 3D radiative effects (cloud side brightening
 520 and darkening) mitigate each other.

521



522

523 **Fig. 8.** Simulated shortwave broadband Reflected flux at top of the domain (F^\uparrow), Transmitted flux at the surface (F^\downarrow) and
 524 Column absorbed flux (F^{abs}) derived from the retrieved clouds properties using 1D RT, F_{1D}^* (a)-(c), derived from the true clouds
 525 properties using 3D RT, F_{3D} (d)-(f), derived from the true clouds properties using 1D RT, F_{1D} (g)-(i) and difference between F_{1D}^*
 526 and F_{1D} (j)-(l) for Solar zenith angle=60° and View zenith angle=0°. Sun is on the Left-hand side of the domain. The solar
 527 irradiance at the top of the domain scales with the cosine of the solar zenith angle.

528 An examination of F_{1D}^\downarrow and $F_{1D}^{*\downarrow}$ for the high sun case reveals that $F_{1D}^{*\downarrow}$ beneath clouds is larger compared
 529 to F_{1D}^\downarrow , while they have same values in clear-sky regions (**Fig. 7k**) This is expected since F_{1D}^{\uparrow} is lesser than
 530 F_{1D}^{\uparrow} . Thus, the amount of $F_{1D}^{*\downarrow}$ at the surface beneath the cloud increases. For the low sun case, F_{1D}^\downarrow and
 531 $F_{1D}^{*\downarrow}$ beneath the clouds have higher values where the TOD reflected flux is low and lower values where
 532 the TOD reflected flux is high (**Fig. 8k**).

533 The radiative quantities across the LES domain have different characteristics in F_{3D} stemming from the
 534 horizontal transport of photons across pixels. For the high sun case, aside the blurriness of the F^\uparrow
 535 component of F_{3D} (denoted by F_{3D}^\uparrow) which was previously explained, an examination of the F^\downarrow
 536 component of F_{3D} (denoted by F_{3D}^\downarrow) map in **Fig. 7e** shows a slight tilt of the cloud shadows according to
 537 the angle of projection of the sun (located at SZA 5° to the left). It also reveals enhanced F_{3D}^\downarrow values
 538 around cloud edges. Such is not the case in F_{1D}^\downarrow (**Fig. 7h**) due to 1D RT setup where each cloudy column is
 539 considered independent. These observations are consistent with findings made by Gristey et al. [2020] for
 540 similar shallow cumulus cloud fields. Gristey et al. [2020], showed that these enhanced F_{3D}^\downarrow around cloud
 541 edges is primarily caused by the diffused component of the transmitted flux which are scattered by clouds
 542 towards clear sky regions beyond cloud shadows. In F_{3D}^\downarrow for the low sun (**Fig. 8e**), due to 3D RT and the
 543 more oblique solar angle (SZA 60°), there is an increase in the total effective cloud cover [Di Giuseppe and

544 Tompkins, 2003; Tompkins and Di Giuseppe, 2007], as well as an increase in the size of the cloud shadow,
 545 which reduces the transmitted flux at the surface (e.g., around [X=7,Y=6 km] in **Fig. 8e**. Just as in the case
 546 of the high sun, these features are absent in the low sun 1D RT runs ($F_{1D}^{*\downarrow}$ and F_{1D}^{\downarrow}). An analysis of the
 547 domain-averaged statistics will help shed more light on the differences between the 3D RT and 1D RT
 548 radiative flux results on the domain scale.

549 **Table 3.** Statistics of successful and failed retrievals from the 3D RT- based radiance for the 27 June and 18 August cloud fields
 550 at Solar zenith angle (SZA) 5 and 60 degrees. The columns from left to right are Case name (Identified by date and time), solar
 551 zenith angle (SZA), Number of pixels with successful retrievals only, Pixels with failed retrievals, Total number of successful and
 552 failed retrievals.

Case Name		SZA 5 degrees			SZA 60 degrees		
		F_{1D}^* (Wm^{-2})	F_{3D} (Wm^{-2})	F_{1D} (Wm^{-2})	F_{1D}^* (Wm^{-2})	F_{3D} (Wm^{-2})	F_{1D} (Wm^{-2})
27 June 2015 (14:00 UTC)	F^\uparrow	215.44 (213.94)	215.93	225.37 (223.52)	134.22 (111.21)	137.87	133.04 (112.01)
	F^\downarrow	918.97 (920.68)	918.79	910.76 (912.88)	419.60 (441.77)	414.36	420.97 (441.34)
	F^{abs}	228.56 (228.37)	228.23	226.82 (226.60)	130.25 (131.13)	131.82	130.11 (130.79)
18 Aug. 2016 (14:00 UTC)	F^\uparrow	315.16 (316.82)	308.68	355.26 (357.12)	209.74 (174.40)	218.62	211.54 (171.59)
	F^\downarrow	805.34 (803.59)	812.25	770.21 (768.26)	342.50 (378.46)	326.53	341.92 (382.68)
	F^{abs}	242.36 (242.48)	241.95	237.36 (237.46)	131.74 (131.20)	138.86	130.55 (129.76)

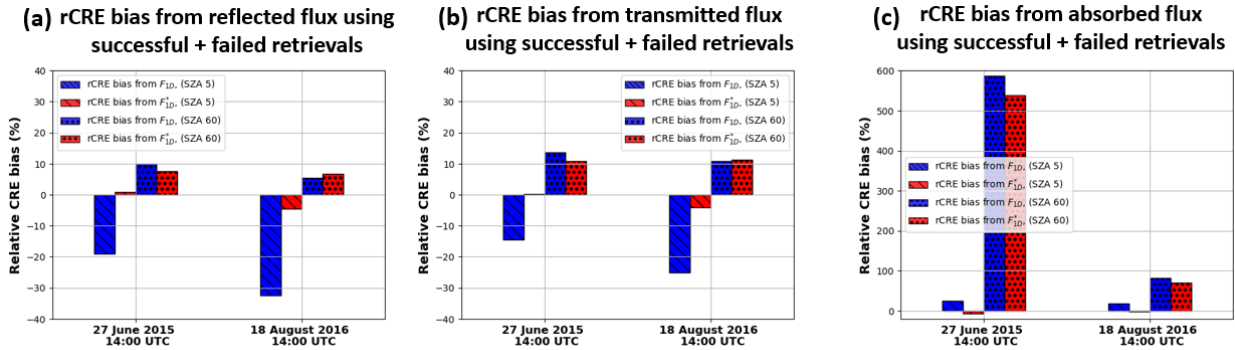
Note: Values before the parentheses are calculated from the combination of failed and successful retrievals representing the total cloudy population, while values in parentheses are calculated from successful retrievals only representing the total cloudy population. clear-sky pixels values have been included in all calculations.

553

554 The domain-averaged broadband F^\uparrow , F^\downarrow and F^{abs} components of F_{1D}^* , F_{1D} and F_{3D} for the 27
 555 June and 18 August cases at SZA 5° and SZA 60° are reported in **Table 3**. As previously explained, the
 556 predominant photon leaking associated with high sun 3D RT and the ensuing underestimation of the
 557 retrieved τ which dominate the cloud property retrievals from high sun 3D simulated reflectance,
 558 increases the number of retrieved optically thinner clouds (relative to the original LES τ used in F_{1D}
 559 calculations) utilized as inputs for the F_{1D}^* calculations. This leads to the underestimation of the
 560 domain-averaged $F_{1D}^{*\uparrow}$ compared to F_{1D}^{\uparrow} ; In the 27 June case, the domain-averaged $F_{1D}^{*\uparrow}$ ($215.44 Wm^{-2}$)
 561 is underestimated compared to the corresponding F_{1D}^{\uparrow} value ($225.37 Wm^{-2}$) by about $9.93 Wm^{-2}$. While
 562 in the 18 August case, the domain-averaged $F_{1D}^{*\uparrow}$ ($315.16 Wm^{-2}$) is underestimated compared to the
 563 corresponding F_{1D}^{\uparrow} value ($355.26 Wm^{-2}$) by $40.1 Wm^{-2}$. The larger value of the underestimated
 564 domain-averaged $F_{1D}^{*\uparrow}$ in the 18 August case stems from its larger cloud fraction and τ bias. The
 565 transmitted flux at the surface below clouds is dependent on the amount of flux reflected towards the
 566 TOD; lower reflected flux values indicate that less radiation is reflected from the clouds, which allows for
 567 a greater amount of radiative flux to be transmitted to the surface beneath the clouds. This reason,
 568 coupled with the overestimation of the transmitted flux at the surface due to missed thin clouds in our
 569 bi-spectral retrievals (red regions in **Fig. 3**, retrieved $\tau = 0$ for VNIR reflectance less than the smallest LUT
 570 τ value), explains why for the high sun case, the domain-averaged $F_{1D}^{*\downarrow}$ values are higher compared to F_{1D}^{\downarrow}
 571 values, resulting in differences of $8.21 Wm^{-2}$ and $35.13 Wm^{-2}$ for the 27 June and 18 August cases
 572 respectively. Although, for the high sun angle, the contribution of the missed thin clouds to the
 573 overestimation of $F_{1D}^{*\downarrow}$ beneath clouds in our case study is small (Constituting about 0.23% and 0.34% of
 574 the domain-averaged surface transmitted flux for the 27 June and 18 August high cases respectively).

575 Comparing results from the three sets of experiments in **Table 3** reveals that for the high sun case,
 576 the F_{1D}^* results clearly agree better with the benchmark F_{3D} , than the F_{1D} results. In the 27 June case, δF_1

577 for the domain-averaged F^\uparrow , F^\downarrow and F^{abs} are 0.49, -0.18 and -0.33 Wm^{-2} respectively, which are
 578 significantly smaller in magnitude than those for δF_2 (-9.44 , 8.03 , and 1.41 Wm^{-2} respectively). Similarly,
 579 for the 18 August case, δF_1 for the domain-averaged F^\uparrow , F^\downarrow and F^{abs} are -6.48 , 6.81 and -0.41 Wm^{-2}
 580 respectively compared to corresponding biases of -46.58 , 42.04 , and 4.59 Wm^{-2} for δF_2 . These results
 581 suggests that F_{1D}^* gives an overall better radiative energy estimate than F_{1D} for the high SZA case. In the
 582 low sun case, the F_{1D}^* and F_{1D} are very close to each other and there is no clear winner when compared
 583 to the benchmark 3D RT results. In the 27 June case, the F_{1D}^* agrees slightly better with 3D results than
 584 the F_{1D} , but the opposite is true in the 18 August case. This result seems to suggest that although in the
 585 low sun case the brightening and darkening effects can lead to large retrieval biases, they tend to cancel
 586 out each other in the flux computations. Interestingly, both 1D results tend to underestimate F^\uparrow and
 587 overestimate F^\downarrow . This is probably because the brightening effect is dominant in the 3D RT leading to some
 588 extremely bright pixels. But they are not captured in the 1D RT computations, even in the F_{1D}^* using the
 589 upper limit of $\tau=158.48$ in the flux computation. Thus, the reflected flux quickly reaches the asymptotic
 590 value when τ is large and therefore simply using larger τ value in 1D RT cannot simulate the extreme
 591 brightness of clouds due the brightening effect in 3D RT. Results for δF_2 computed from the transmitted
 592 flux at the surface for both cloud cases (27 June and 18 August) are positive when the sun is high (8.03
 593 and 42.04 Wm^{-2}) and negative for the low sun angle (-6.61 and -15.39 Wm^{-2}) consistent with Gristey
 594 el al. [2020] study for surface irradiance showing positive domain mean δF_2 in the afternoon (high sun)
 595 and negative domain mean δF_2 towards the end of the day (low sun).



596

597 **Fig. 9.** Relative cloud radiative effect (rCRE) bias computed from the successful + failed retrievals (a) top of the domain
 598 reflected, (b) surface transmitted and (c) absorbed flux for the two cloud fields.

599 Because both cloud cases have a cloud fraction lower than 50%, the domain-averaged statistics
 600 include a large fraction of clear-sky pixels. Now we focus our scope on cloudy pixels and investigate the
 601 differences in CRE. The rCRE bias provides a quantitative estimate of how these biases affect the CRE. For
 602 the two cloud cases considered in this study, plots of rCRE bias computed from the F^\uparrow , F^\downarrow and F^{abs} at SZA
 603 5° and 60° for F_{1D}^* and F_{1D} relative to F_{3D} are presented in **Fig. 9**. In the 27 June case, the rCRE bias of
 604 0.97% computed from the high sun $F_{1D}^{*\uparrow}$ result indicate a negligible deviation (less than 1%) from the
 605 benchmark CRE while the rCRE bias of -19% computed from the high sun F_{1D}^\uparrow result show that the bias
 606 is quite substantial. Similarly, for the 18 August case, the rCRE bias computed from the high sun $F_{1D}^{*\uparrow}$ result
 607 is less than 5%. On the other hand, the rCRE bias of -32.48% computed from the high sun F_{1D}^\uparrow result
 608 show that the bias is quite large. Similar results are obtained for rCRE bias computed from F^\downarrow . In the 27
 609 June case, the rCRE bias computed from the $F_{1D}^{*\downarrow}$ is 0.33% (**Fig. 9b**, second bar on the left) which shows

610 minimal bias less than 1%, while the rCRE computed from the F_{1D}^\downarrow is -14.5% (**Fig. 9b**, first bar on the left).
611 Similarly, for the 18 August case, the rCRE bias computed from the F_{1D}^\downarrow is -4.12% (**Fig. 9b**, second bar on the
612 right), while the rCRE bias computed from the F_{1D}^\downarrow is -25.10% (**Fig. 9b**, first bar on the right).

613 When the absorbed flux is taken into consideration, for the 27 June high sun case, the rCRE bias computed
614 from the absorbed component of F_{1D}^* (F_{1D}^{*abs}) is -6.05% (**Fig. 9c**, second bar on the left) which is less bias
615 compared to the 25.64% rCRE bias computed from the absorbed component of F_{1D} (F_{1D}^{abs}) (**Fig. 9c**, first
616 bar on the left). Similarly, for the 18 August case, the rCRE bias computed from F_{1D}^{*abs} is -1.73% (**Fig. 9c**,
617 second bar on the right), while the rCRE bias computed from F_{1D}^{abs} is 19.09% (**Fig. 9c**, first bar on the right).
618 For the low sun case, the rCRE biases computed from F_{1D}^* and F_{1D} are comparable, which is consistent
619 with the domain-averaged statistics in **Table 3**. Evidently, both F_{1D}^* and F_{1D} overestimate the CRE at TOD
620 and surface, which means an underestimation of cloud reflection and overestimation of transmission. This
621 is consistent with the results in **Table 3**.

622 Overall, the above analysis indicates that the F_{1D}^* provides a better (in the high sun case) or at least
623 comparable (in the low sun case) results than F_{1D} for both domain-averaged flux statistics and CRE when
624 compared to the benchmark F_{3D} results. With these results we can conclude that the CRE calculated with
625 1D RT using retrieved cloud properties which are biased due to the 3D effects is found to be comparable
626 or better than the CRE calculated with 1D RT using the true cloud properties.

627 **4. Summary and Conclusion**

628 It is well known that the bi-spectral cloud property retrievals based on the 1D RT have significant
629 errors due to the 3D radiative effects. In this study, we investigate whether the biased retrievals can still
630 be used to estimate the broadband flux and CRE. To address this question, we selected two cloud fields
631 from the LASSO activity: one on 27 June 2015 and another on 18 August 2016 to serve as case studies for
632 our research. The LES cloud fields have different microphysics with different CBH, CTH and the value of
633 the cloud fraction for the 18 August 2016 cloud field (47.08%) is more than twice that of the 27 June 2015
634 (20.15%) cloud field. Radiance simulations, bi-spectral retrievals, and broadband SW flux radiative transfer
635 simulations were performed using these cloud fields at two SZAs, a high sun case ($SZA=5^\circ$) and a low sun
636 case ($SZA=60^\circ$) and the results were analyzed. The flux computations were carried out in three sets, the
637 reference broadband SW flux calculations were performed using the cloud properties from the original
638 LES cloud field under 3D RT (F_{3D}), we also computed similar RT broadband SW flux calculations with the
639 same cloud properties from the original LES cloud field except that the RT calculations were computed
640 using 1D RT (F_{1D}). Additionally, we computed the last set of broadband SW flux calculations using 1D RT
641 and bi-spectrally retrieved cloud properties as inputs (F_{1D}^*).

642 The high sun radiance results, for the two cloud fields show that in 3D RT high sun case, the photons
643 leaking from optically thick cloudy regions to optically thin cloudy regions and surface dominate the LES
644 reflectance field. These results in overestimated r_e and underestimated τ dominating the cloud property
645 retrievals. While results from the low sun case, for the two cloud fields considered show that in
646 comparison to the 1D RT radiance fields, brightening and darkening effects both occur in the 3D RT
647 simulated radiance observation. Therefore, retrievals from the low sun 3D radiance observations are
648 characterized mainly by both overestimation of τ and underestimation of r_e in brightened pixels and
649 underestimation of τ and overestimation of r_e in darkened pixels. The cumulative effects of these

650 brightening and darkening/Photon leaking effects and its impacts on the retrieved cloud properties
651 dictates their impact on the broadband radiative flux.

652 The results from the broadband SW radiative fluxes computation showed that, although the
653 bi-spectrally retrieved cloud properties are often biased due to the 3D radiative transfer effects, for high
654 sun cases, calculations of the CRE from these F_{1D}^* values agree well with the benchmark values (which is
655 the F_{3D} in our case) with agreement within 7% for rCRE bias calculations from the reflected, transmitted
656 and absorbed fluxes in the high sun cases. Conversely, the rCRE bias computed from the F_{1D} quantities
657 could reach about 33%. Thus, for high sun situations, the F_{1D}^* provides consistently better estimates of
658 the CRE than the F_{1D} . For the low sun case, the two 1D RT experiments provide comparable results, both
659 underestimating cloud reflection and overestimating transmission, and there is not a clear winner when
660 compared to the 3D RT benchmark.

661 The influence of the failed retrievals on the CRE was also investigated (see details in Appendix),
662 with results indicating that for the high sun case, the impact of the failed retrievals on the radiative flux
663 quantities is negligible, with less than 6% changes observed in the rCRE bias computed from the
664 domain-averaged TOD reflected, surface transmitted and absorbed F_{1D}^* and F_{1D} results. Such is not the
665 case for the low sun case where the failed retrievals have a very huge impact on the radiative flux
666 quantities. Excluding the failed retrievals from the domain-averaged reflected, transmitted, and absorbed
667 F_{1D}^* and F_{1D} low sun case analysis could increase the rCRE bias by a as much as factor of 6 compared to
668 values which included the failed retrievals in the analysis. Whether or not to always use the failed
669 retrievals in the radiative flux and CRE estimation is still an important question, especially how best to
670 filter out the failed retrievals from cloud properties retrieved from instruments that rely on bi-spectral
671 method (e.g., in MODIS cloud products) for use in radiative flux estimation? We observed here that,
672 filtering out all failed retrievals, especially from the low sun angle can greatly impact the radiative flux
673 estimates. Thus, efforts should be conducted to study which category of failed retrievals is most relevant
674 for use in CRE estimation.

675 In conclusion, despite the potential biases due to the 3D radiative effects, the retrieved cloud
676 properties based on 1D RT from the bi-spectral method still provide CRE estimates that are comparable
677 to or better than CRE calculated from the true cloud properties using 1D RT. Some future questions that
678 warrant answers involves how the 3D radiative effects affect the broadband fluxes for different cloud
679 arrangements and other types of clouds, such as deep convective clouds. Also, while we have considered
680 only nadir view angle in this work, previous studies [e.g., Várnai and Marshak, 2007] have shown that the
681 biases of 1D cloud retrievals vary systematically with view direction, therefore, the impacts of off-nadir
682 view directions on the broadband flux need to be investigated. Another important study will be to
683 determine how changes in surface albedo and type affect our results. Additionally, while our case study
684 mainly focused on the impact of the 3D radiative effects on SW fluxes, the impact of the 3D radiative
685 effects on LW radiation is important and needs to be investigated.

686 **Appendix A: Impacts of failed retrievals on the radiative flux**

687 The calculations of F_{1D}^* and domain radiative flux analysis in Sect. 3.3 utilized both the successful
688 and failed retrievals (categorized in Sect. 2.4) to represent the total population of cloudy pixels.
689 Henceforth, both successful and failed retrievals as a representative of the total population of cloudy
690 pixels will be referred to as “all retrieved cloud pixels”. In this appendix, our focus is to examine and

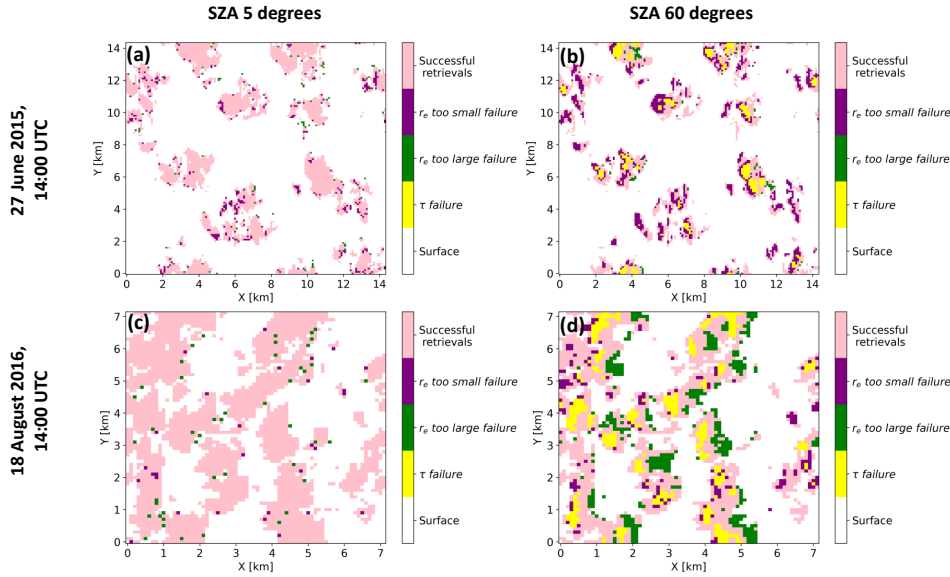
691 compare the TOD reflected, surface transmitted and column absorbed radiative fluxes, when the failed
692 retrievals are excluded from the radiative flux analysis. This will help to diagnose if using solely successful
693 retrievals as a representative of the total population of cloudy pixels in the LES domain will produce the
694 correct radiative energy estimates and thus provide information on the radiative properties of the
695 excluded failed retrievals.

696 An examination of the high sun domain-averaged F^\uparrow , F^\downarrow and F^{abs} for both LES cloud cases, when
697 only successful retrievals represent the total population of cloudy pixels in the F_{1D}^* calculations, show
698 minimal changes (within the range $\pm 1.9 \text{ Wm}^{-2}$) from previous values which utilized all retrieved cloud
699 pixels in the radiative flux analysis (**Table 3**). This is due to the small number of failed retrievals in the high
700 sun scenario ($< 14\%$ for both cloud cases; **Table 2**). But this is not the case for the low sun case, where
701 changes between the two aforementioned calculations are large, reaching up to $\pm 35.96 \text{ Wm}^{-2}$ (**Table 3**).
702 These large changes are because of the large number of failed retrievals from strong 3D radiative effects
703 ($> 43\%$ for both cloud cases; **Table 2**) as well as different radiative behavior of the failed retrievals
704 categories observed in the low sun scenario. **Fig. A1** shows plots of successful and failed retrievals
705 categories (classified as described in Sect. 2.4) from the high and low sun radiance for the 27 June and 18
706 August cases. From these plots, it is observed that when the SZA is 60° , the r_e too small failures are
707 predominant around cloud edges in the sunlit areas. The τ failures are observed mostly in the illuminated
708 sunlit cloudy regions and the r_e too large failures occur mostly on the opposite sides where the shadowing
709 effect is dominant (**Fig. A1b** and **d**). For the high sun at SZA 5° , τ failures are almost negligible because the
710 VNIR reflectance observations does not exceed the LUT τ upper limit of 158.48, while there is a small
711 number of occurrences of the r_e too large and r_e too small failures (**Fig. A1a** and **c**).

712 It should be noted that when we exclude the failed retrievals from the broadband flux analysis,
713 we keep the total cloud fraction constant. In other words, we scale the broadband flux based on the
714 successful pixels by the ratio of total cloudy to successful pixels such that the effect of cloud fraction
715 reduction is removed from the analysis. The impacts of excluding failed retrievals on the domain-averaged
716 broadband flux can be assessed by comparing the values outside the parentheses with those inside in
717 **Table 3**, and better understood in the light of failed retrieval statistics given in **Table 2**.

718 Results of F_{1D}^* for the 27 June case at SZA 5° , show that the domain - averaged F_{1D}^{\uparrow} is
719 underestimated by 1.50 Wm^{-2} (213.94 Wm^{-2} in comparison to 215.44 Wm^{-2}) when only successful
720 pixels are used to represent the total population of cloudy pixels compared to results which utilize all
721 retrieved cloud pixels in the radiative flux analysis. This is mainly because the dominant type of retrieval
722 failure in this case is the r_e too small failure, accounting for about 71% of the failed pixel retrieval statistics
723 (see **Table 2**). Recall that r_e too small failure is mainly a result of brightening effect and therefore
724 associated pixels appear brighter in 3D RT than 1D RT. As a result, excluding these pixels leads to an
725 underestimate of domain-averaged broadband reflected flux. For the same reason, excluding these pixels
726 leads to an overestimation of transmitted flux at the domain bottom.

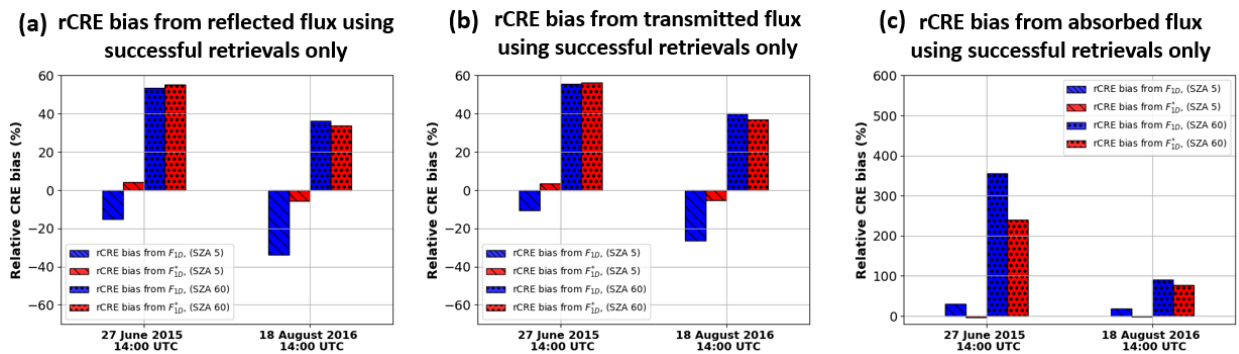
727 In contrast to the 27 June case, excluding the failed retrievals in the F_{1D}^* for the 18 August case
728 leads to an overestimation of domain-averaged F_{1D}^{\uparrow} and underestimation of the F_{1D}^{\downarrow} . This is probably
729 because the dominant failed retrieval type is the r_e too large which is because of the darkening effect.
730 These pixels appear darker from the perspective of TOD and more transmissive from the perspective of
731 bottom in 3D RT than 1D RT. For comparison purpose, we have also excluded the failed pixels from the
732 F_{1D} calculations. Overall, the results are very similar and consistent with those based on F_{1D}^* .



733

734 **Fig A1.** Plots of successful and failed retrievals categories for the 27 June 2015 and 18 August 2016 cases at Solar zenith angle 5
 735 degrees (a and c) and Solar zenith angle 60 degrees (b and d).

736 In comparison with the high sun case, the impacts of failed retrievals on the broadband flux
 737 statistics are much larger in the low sun SZA 60° case. In both LES cases, the exclusion of failed retrievals
 738 leads to a significant decrease of domain-averaged $F_{1D}^{*\uparrow}$ and increase of the $F_{1D}^{*\downarrow}$. For example, in the 27
 739 June case, the $F_{1D}^{*\uparrow}$ decreased from 134.22 Wm^{-2} when failed pixels are included to 111.21 Wm^{-2} when
 740 they are excluded, which is accompanied by an increase of the $F_{1D}^{*\downarrow}$ from 419.60 Wm^{-2} to 441.77 Wm^{-2} .
 741 A close look at **Table 2** reveals that in both LES cases, the combination of r_e too small and τ failures
 742 accounts for the majority of failed retrievals, 95% in the case of 27 June and 68% in the 18 August case.
 743 As mentioned above, both types of failures are because of the brightening effect. Excluding them is
 744 expected to cause underestimation of domain-averaged reflected flux and overestimation of the
 745 transmitted flux.



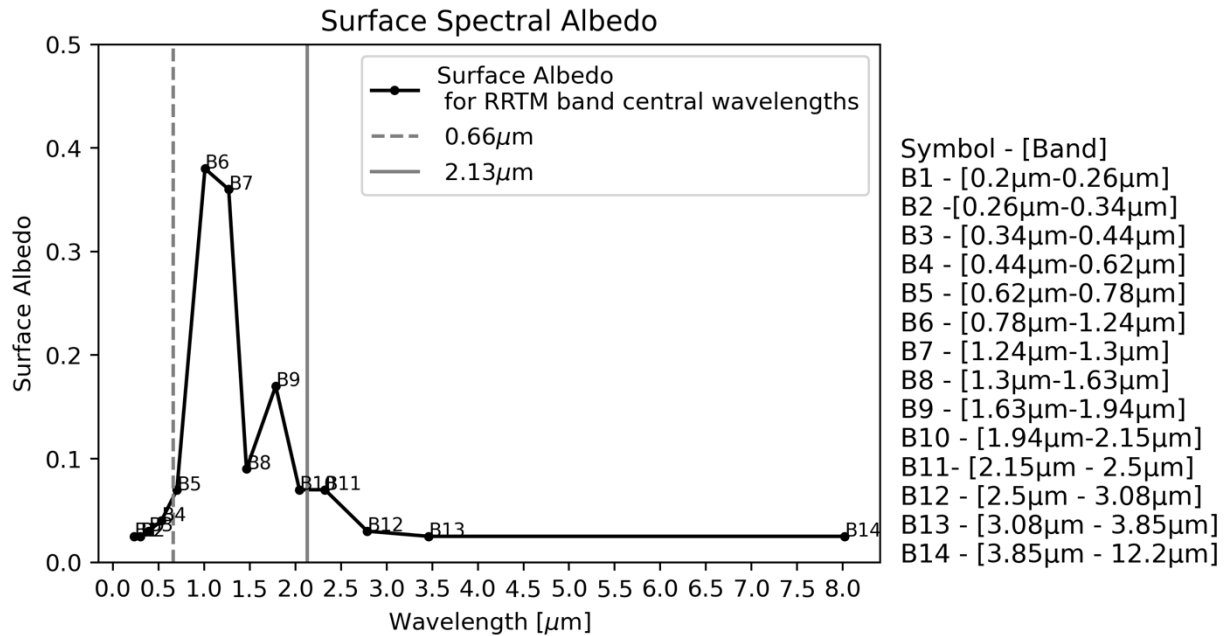
746

747 **Fig.A2.** Relative cloud radiative effect bias computed from the successful only retrievals, top of the domain reflected in (a), surface
 748 transmitted in (b) and column absorbed flux in (c) for the two cloud fields.

749 The impacts of excluding failed retrievals on the rCRE bias are shown in **Fig. A2**. A comparison to
 750 the results in **Fig. 9** reveals two points. First, the biases in the low sun cases become much larger which is
 751 expected because there are much more failed retrievals in these cases. Second, it is evident that the flux

752 estimates derived from the retrieved clouds using 1D RT still provide a better (in case of high sun) or
 753 comparable (in case of low sun) approximation to the flux estimates from the true cloud fields using 3D
 754 RT simulations in comparison with those derived from the true cloud fields using 1D RT. Therefore, our
 755 conclusion made based on the statistics of all retrievals still holds when failed retrievals are excluded from
 756 the analysis. On the other hand, it is also evident that to achieve a better comparison with the flux derived
 757 from the true clouds using 3D RT, it is better to include the failed retrievals to preserve the effects of 3D
 758 RT.

759 **Appendix B: Surface spectral Albedo plot**



760
 761 Fig.B1. Surface spectral albedo plot utilized in the study. B_i (i ranges from 1 to 14) represent the bands which are in parenthesis.

762 **Code/Data availability**

763 The radiative transfer models and data used in the study are publicly available online. The I3RC
 764 Community Monte Carlo Radiative Transfer Model is freely available at
 765 <https://github.com/RobertPincus/i3rc-monte-carlo-model>, while the SHDOM radiative transfer code is
 766 freely available from <https://coloradolinux.com/shdom/> (The SHDOM is described in detail in a journal
 767 article available at [https://doi.org/10.1175/15200469\(1998\)055<0429:TSHDOM>2.0.CO;2](https://doi.org/10.1175/15200469(1998)055<0429:TSHDOM>2.0.CO;2) [Evans, 1998]).
 768 The LASSO LES data utilized for the study can be accessed at <https://archive.arm.gov/lassobrowser>. The
 769 Post-processed LES fields utilized as inputs for radiative transfer are available at
 770 <https://zenodo.org/doi/10.5281/zenodo.10511731>.

771 **Author contribution**

772 Conceptualization, Z.Z.; methodology, A.S.A., Z.Z. ; software, A.S.A., Z.Z., ; validation, A.S.A. and Z.Z.;
 773 formal analysis, A.S.A.; investigation, A.S.A., and Z.Z.; data curation, A.S.A, Z.Z; writing–original draft
 774 preparation, A.S.A.; writing–review and editing, A.S.A.,Z.H.T., J.Z., C.W., S.P., J.W., K.G.M., T.V., Z.Z.;

775 visualization; A.S.A.; supervision, Z.Z.; project administration, Z.Z.; funding acquisition, Z.Z., J.W., K.G.M.,
776 C.W. All authors have read and agreed to the published version of the manuscript.

777 **Competing interest**

778 The contact author has declared that none of the authors has any competing interests.

779 **Acknowledgements**

780 This research has been supported by the NASA ACCESS project (grant no. 80NSSC21M0027). The
781 computations for this study have been performed by the UMBC High Performance Computing Facility
782 (HPCF). The facility is supported by the US National Science Foundation through the MRI program (grant
783 nos. CNS-0821258 and CNS-1228778) and the SCREMS program (grant no. DMS-0821311), with
784 substantial support from UMBC.
785

786 **References**

- 787
788 Atmospheric Radiation Measurement (ARM) user facility. 2015. LES ARM Symbiotic Simulation and
789 Observation (LASSO) (LASSODIAGRAW108). 2015-06-27 to 2015-06-27, Southern Great Plains
790 (SGP) Central Facility, Lamont, OK (C1). Compiled by W. Gustafson, A. Vogelmann, X. Cheng, S.
791 Endo, B. Krishna, Z. Li, T. Toto, H. Xiao and K. Johnson. ARM Data Center. Data set accessed 2022-
792 11-08 at <http://dx.doi.org/10.5439/1342961>.
- 793 Atmospheric Radiation Measurement (ARM) user facility. 2016. LES ARM Symbiotic Simulation and
794 Observation (LASSO) (LASSODIAGRAW113). 2016-08-18 to 2016-08-18, Southern Great Plains
795 (SGP) Central Facility, Lamont, OK (C1). Compiled by W. Gustafson, A. Vogelmann, X. Cheng, S.
796 Endo, B. Krishna, Z. Li, T. Toto, H. Xiao and K. Johnson. ARM Data Center. Data set accessed 2023-
797 05-19 at <http://dx.doi.org/10.5439/1342961>.
- 798 Barker, H. W., Jerg, M. P., Wehr, T., Kato, S., Donovan, D. P., and Hogan, R. J.: A 3D cloud-construction
799 algorithm for the EarthCARE satellite mission, Quarterly Journal of the Royal Meteorological
800 Society, 137, 1042-1058, <https://doi.org/10.1002/qj.824>, 2011.
- 801 Barker, H. W., Kato, S., and Wehr, T.: Computation of Solar Radiative Fluxes by 1D and 3D Methods Using
802 Cloudy Atmospheres Inferred from A-train Satellite Data, Surveys in Geophysics, 33, 657-676,
803 <https://doi.org/10.1007/s10712-011-9164-9>, 2012.
- 804 Cho, H.-M., Zhang, Z., Meyer, K., Lebsock, M., Platnick, S., Ackerman, A. S., Di Girolamo, L., C.-Labonnote,
805 L., Cornet, C., Riedi, J., and Holz, R. E.: Frequency and causes of failed MODIS cloud property
806 retrievals for liquid phase clouds over global oceans, Journal of Geophysical Research:
807 Atmospheres, 120, 4132-4154, <https://doi.org/10.1002/2015JD023161>, 2015.
- 808 Coddington, O., Pilewskie, P., Schmidt, K. S., McBride, P. J., and Vukicevic, T.: Characterizing a New
809 Surface-Based Shortwave Cloud Retrieval Technique, Based on Transmitted Radiance for Soil and
810 Vegetated Surface Types, <https://doi.org/10.3390/atmos4010048>, 2013.
- 811 Davis, A. B. and Marshak, A.: Multiple Scattering in Clouds: Insights from Three-Dimensional Diffusion/P1
812 Theory, Nuclear Science and Engineering, 137, 251-280, <https://doi.org/10.13182/NSE01-A2190>,
813 2001.
- 814 Di Giuseppe, F. and Tompkins, A. M.: Three-dimensional radiative transfer in tropical deep convective
815 clouds, Journal of Geophysical Research: Atmospheres, 108,
816 <https://doi.org/10.1029/2003JD003392>, 2003.
- 817 Evans, K. F.: The Spherical Harmonics Discrete Ordinate Method for Three-Dimensional Atmospheric
818 Radiative Transfer, Journal of the Atmospheric Sciences, 55, 429-446,
819 [https://doi.org/10.1175/1520-0469\(1998\)055<0429:TSHDOM>2.0.CO;2](https://doi.org/10.1175/1520-0469(1998)055<0429:TSHDOM>2.0.CO;2), 1998.

820 Gristey, J. J., Feingold, G., Schmidt, K. S., and Chen, H.: Influence of Aerosol Embedded in Shallow Cumulus
821 Cloud Fields on the Surface Solar Irradiance, *Journal of Geophysical Research: Atmospheres*, 127,
822 e2022JD036822, <https://doi.org/10.1029/2022JD036822>, 2022.

823 Gristey, J. J., Feingold, G., Glenn, I. B., Schmidt, K. S., and Chen, H.: Surface Solar Irradiance in Continental
824 Shallow Cumulus Fields: Observations and Large-Eddy Simulation, *Journal of the Atmospheric
825 Sciences*, 77, 1065-1080, <https://doi.org/10.1175/JAS-D-19-0261.1>, 2020.

826 Gustafson, W. I., Vogelmann, A. M., Li, Z., Cheng, X., Dumas, K. K., Endo, S., Johnson, K. L., Krishna, B.,
827 Fairless, T., and Xiao, H.: The Large-Eddy Simulation (LES) Atmospheric Radiation Measurement
828 (ARM) Symbiotic Simulation and Observation (LASSO) Activity for Continental Shallow
829 Convection, *Bulletin of the American Meteorological Society*, 101, E462-E479,
830 <https://doi.org/10.1175/BAMS-D-19-0065.1>, 2020.

831 Hogan, R. J., Fielding, M. D., Barker, H. W., Villefranche, N., and Schäfer, S. A. K.: Entrapment: An
832 Important Mechanism to Explain the Shortwave 3D Radiative Effect of Clouds, *Journal of the
833 Atmospheric Sciences*, 76, 2123-2141, <https://doi.org/10.1175/JAS-D-18-0366.1>, 2019.

834

835 Kato, S., Rose, F. G., Sun-Mack, S., Miller, W. F., Chen, Y., Rutan, D. A., Stephens, G. L., Loeb, N. G., Minnis,
836 P., Wielicki, B. A., Winker, D. M., Charlock, T. P., Stackhouse Jr, P. W., Xu, K.-M., and Collins, W.
837 D.: Improvements of top-of-atmosphere and surface irradiance computations with CALIPSO-
838 CloudSat-, and MODIS-derived cloud and aerosol properties, *Journal of Geophysical Research:
839 Atmospheres*, 116, <https://doi.org/10.1029/2011JD016050>, 2011.

840 Kay, J. E., Hillman, B. R., Klein, S. A., Zhang, Y., Medeiros, B., Pincus, R., Gettelman, A., Eaton, B., Boyle, J.,
841 Marchand, R., and Ackerman, T. P.: Exposing Global Cloud Biases in the Community Atmosphere
842 Model (CAM) Using Satellite Observations and Their Corresponding Instrument Simulators,
843 *Journal of Climate*, 25, 5190-5207, <https://doi.org/10.1175/JCLI-D-11-00469.1>, 2012.

844 Kiehl, J. T. and Trenberth, K. E.: Earth's Annual Global Mean Energy Budget, *Bulletin of the American
845 Meteorological Society*, 78, 197-208, [https://doi.org/10.1175/1520-0477\(1997\)078<0197:EAGMEB>2.0.CO;2](https://doi.org/10.1175/1520-0477(1997)078<0197:EAGMEB>2.0.CO;2), 1997.

846

847 Levis, A., Schechner, Y. Y., Aides, A., and Davis, A. B.: Airborne Three-Dimensional Cloud Tomography,
848 2015 IEEE International Conference on Computer Vision (ICCV), 7-13 Dec. 2015, 3379-3387,
849 10.1109/ICCV.2015.386,

850 Liou, K. N.: Radiation and Cloud Processes in the Atmosphere: Theory, Observation, and Modeling,
851 <https://doi.org/10.1093/oso/9780195049107.001.0001>, 1992.

852 Loeb, N. G. and Manalo-Smith, N.: Top-of-Atmosphere Direct Radiative Effect of Aerosols over Global
853 Oceans from Merged CERES and MODIS Observations, *Journal of Climate*, 18, 3506-3526,
854 <https://doi.org/10.1175/JCLI3504.1>, 2005.

855 Loveridge, J., Levis, A., Di Girolamo, L., Holodovsky, V., Forster, L., Davis, A. B., and Schechner, Y. Y.:
856 Retrieving 3D distributions of atmospheric particles using Atmospheric Tomography with 3D
857 Radiative Transfer – Part 1: Model description and Jacobian calculation, *Atmos. Meas. Tech.*, 16,
858 1803-1847, 10.5194/amt-16-1803-2023, 2023.

859 Marshak, A. and Davis, A. B.: Horizontal Fluxes and Radiative Smoothing, in: 3D Radiative Transfer in
860 Cloudy Atmospheres, edited by: Marshak, A., and Davis, A., Springer Berlin Heidelberg, Berlin,
861 Heidelberg, 543-586, 10.1007/3-540-28519-9_12, 2005.

862 Marshak, A., Platnick, S., Várnai, T., Wen, G., and Cahalan, R. F.: Impact of three-dimensional radiative
863 effects on satellite retrievals of cloud droplet sizes, *Journal of Geophysical Research:
864 Atmospheres*, 111, <https://doi.org/10.1029/2005JD006686>, 2006.

865 Masuda, R., Iwabuchi, H., Schmidt, K. S., Damiani, A., and Kudo, R.: Retrieval of Cloud Optical Thickness
866 from Sky-View Camera Images using a Deep Convolutional Neural Network based on Three-
867 Dimensional Radiative Transfer, <https://doi.org/10.3390/rs11171962>, 2019.

868 Miller, D. J., Zhang, Z., Ackerman, A. S., Platnick, S., and Baum, B. A.: The impact of cloud vertical profile
869 on liquid water path retrieval based on the bispectral method: A theoretical study based on large-

870 eddy simulations of shallow marine boundary layer clouds, *Journal of Geophysical Research: Atmospheres*, 121, 4122-4141, <https://doi.org/10.1002/2015JD024322>, 2016.

871

872 Miller, D. J., Zhang, Z., Platnick, S., Ackerman, A. S., Werner, F., Cornet, C., and Knobelspiesse, K.:

873 Comparisons of bispectral and polarimetric retrievals of marine boundary layer cloud

874 microphysics: case studies using a LES–satellite retrieval simulator, *Atmos. Meas. Tech.*, 11, 3689-

875 3715, 10.5194/amt-11-3689-2018, 2018.

876 Mlawer, E. J., Taubman, S. J., Brown, P. D., Iacono, M. J., and Clough, S. A.: Radiative transfer for

877 inhomogeneous atmospheres: RRTM, a validated correlated-k model for the longwave, *Journal*

878 *of Geophysical Research: Atmospheres*, 102, 16663-16682, <https://doi.org/10.1029/97JD00237>,

879 1997.

880 Morrison, H. and Gettelman, A.: A new two-moment bulk stratiform cloud microphysics scheme in the

881 Community Atmosphere Model, version 3 (CAM3). Part I: Description and numerical tests,

882 *Journal of Climate*, 21, 3642-3659, 2008.

883 Nakajima, T. and King, M. D.: Determination of the Optical Thickness and Effective Particle Radius of

884 Clouds from Reflected Solar Radiation Measurements. Part I: Theory, *Journal of Atmospheric*

885 *Sciences*, 47, 1878-1893, [https://doi.org/10.1175/1520-](https://doi.org/10.1175/1520-0469(1990)047<1878:DOTOTA>2.0.CO;2)

886 [0469\(1990\)047<1878:DOTOTA>2.0.CO;2](https://doi.org/10.1175/1520-0469(1990)047<1878:DOTOTA>2.0.CO;2), 1990.

887 Nam, C., Bony, S., Dufresne, J. L., and Chepfer, H.: The ‘too few, too bright’ tropical low-cloud problem in

888 CMIP5 models, *Geophysical Research Letters*, 39, <https://doi.org/10.1029/2012GL053421>, 2012.

889 Nataraja, V., Schmidt, S., Chen, H., Yamaguchi, T., Kazil, J., Feingold, G., Wolf, K., and Iwabuchi, H.:

890 Segmentation-based multi-pixel cloud optical thickness retrieval using a convolutional neural

891 network, *Atmos. Meas. Tech.*, 15, 5181-5205, <https://doi.org/10.5194/amt-15-5181-2022>, 2022.

892 Okamura, R., Iwabuchi, H., and Schmidt, K. S.: Feasibility study of multi-pixel retrieval of optical thickness

893 and droplet effective radius of inhomogeneous clouds using deep learning, *Atmos. Meas. Tech.*,

894 10, 4747-4759, 10.5194/amt-10-4747-2017, 2017.

895 Okata, M., Nakajima, T., Suzuki, K., Inoue, T., Nakajima, T. Y., and Okamoto, H.: A study on radiative

896 transfer effects in 3-D cloudy atmosphere using satellite data, *Journal of Geophysical Research: Atmospheres*,

897 122, 443-468, <https://doi.org/10.1002/2016JD025441>, 2017.

898 Oreopoulos, L., Cho, N., Lee, D., and Kato, S.: Radiative effects of global MODIS cloud regimes, *Journal of*

899 *Geophysical Research: Atmospheres*, 121, 2299-2317, <https://doi.org/10.1002/2015JD024502>,

900 2016.

901 O’Hirok, W. and Gautier, C.: A Three-Dimensional Radiative Transfer Model to Investigate the Solar

902 Radiation within a Cloudy Atmosphere. Part I: Spatial Effects, *Journal of the Atmospheric*

903 *Sciences*, 55, 2162-2179, [https://doi.org/10.1175/1520-](https://doi.org/10.1175/1520-0469(1998)055<2162:ATDRTM>2.0.CO;2)

904 [0469\(1998\)055<2162:ATDRTM>2.0.CO;2](https://doi.org/10.1175/1520-0469(1998)055<2162:ATDRTM>2.0.CO;2), 1998.

905 Pincus, R. and Evans, K. F.: Computational Cost and Accuracy in Calculating Three-Dimensional Radiative

906 Transfer: Results for New Implementations of Monte Carlo and SHDOM, *Journal of the*

907 *Atmospheric Sciences*, 66, 3131-3146, <https://doi.org/10.1175/2009JAS3137.1>, 2009.

908 Platnick, S., King, M. D., Ackerman, S. A., Menzel, W. P., Baum, B. A., Riedi, J. C., and Frey, R. A.: The MODIS

909 cloud products: algorithms and examples from Terra, *IEEE Transactions on Geoscience and*

910 *Remote Sensing*, 41, 459-473, <https://doi.org/10.1109/TGRS.2002.808301>, 2003.

911 Platnick, S., Meyer, K. G., King, M. D., Wind, G., Amarasinghe, N., Marchant, B., Arnold, G. T., Zhang, Z.,

912 Hubanks, P. A., and Holz, R. E.: The MODIS cloud optical and microphysical products: Collection

913 6 updates and examples from Terra and Aqua, *IEEE Transactions on Geoscience and Remote*

914 *Sensing*, 55, 502-525, 2016.

915 Rajapakshe, C. and Zhang, Z.: Using polarimetric observations to detect and quantify the three-

916 dimensional radiative transfer effects in passive satellite cloud property retrievals: Theoretical

917 framework and feasibility study, *Journal of Quantitative Spectroscopy and Radiative Transfer*,

918 246, 106920, <https://doi.org/10.1016/j.jqsrt.2020.106920>, 2020.

919 Ramanathan, V., Cess, R. D., Harrison, E. F., Minnis, P., Barkstrom, B. R., Ahmad, E., and Hartmann, D.:

920 Cloud-Radiative Forcing and Climate: Results from the Earth Radiation Budget Experiment,
 921 Science, 243, 57-63, 10.1126/science.243.4887.57, 1989.

922 Rossow, W. B. and Schiffer, R. A.: Advances in Understanding Clouds from ISCCP, Bulletin of the American
 923 Meteorological Society, 80, 2261-2288, [https://doi.org/10.1175/1520-0477\(1999\)080<2261:AIUCFI>2.0.CO;2](https://doi.org/10.1175/1520-0477(1999)080<2261:AIUCFI>2.0.CO;2), 1999.

924
 925 Singer, C. E., Lopez-Gomez, I., Zhang, X., and Schneider, T.: Top-of-Atmosphere Albedo Bias from
 926 Neglecting Three-Dimensional Cloud Radiative Effects, Journal of the Atmospheric Sciences, 78,
 927 4053-4069, <https://doi.org/10.1175/JAS-D-21-0032.1>, 2021.

928 Song, H., Zhang, Z., Ma, P.-L., Ghan, S. J., and Wang, M.: An Evaluation of Marine Boundary Layer Cloud
 929 Property Simulations in the Community Atmosphere Model Using Satellite Observations:
 930 Conventional Subgrid Parameterization versus CLUBB, Journal of Climate, 31, 2299-2320,
 931 <https://doi.org/10.1175/JCLI-D-17-0277.1>, 2018.

932 Stephens, G. L.: The transfer of radiation through vertically nonuniform stratocumulus water clouds,
 933 Radiation in the Atmosphere, 184, 1977.

934 Stocker, T. F., D. Qin, G.-K. Plattner, M. Tignor, S.K. Allen, J. Boschung, A. Nauels, Y. Xia, V. Bex and P.M.
 935 Midgley (eds.: IPCC, 2013: *Climate Change 2013: The Physical Science Basis. Contribution of*
 936 *Working Group I to the Fifth Assessment Report of the Intergovernmental Panel on Climate*
 937 *Change.*, Cambridge University Press, Cambridge, United Kingdom and New York, NY, USA, 1535
 938 pp., 2013.

939 Tompkins, A. M. and Di Giuseppe, F.: Generalizing Cloud Overlap Treatment to Include Solar Zenith Angle
 940 Effects on Cloud Geometry, Journal of the Atmospheric Sciences, 64, 2116-2125,
 941 <https://doi.org/10.1175/JAS3925.1>, 2007.

942 Trenberth, K. E., Fasullo, J. T., and Kiehl, J.: Earth's Global Energy Budget, Bulletin of the American
 943 Meteorological Society, 90, 311-324, <https://doi.org/10.1175/2008BAMS2634.1>, 2009.

944

945 Vardavas, I. and Taylor, F.: Radiation and Climate: Atmospheric energy budget from satellite remote
 946 sensing, International Monographs on Ph2011.

947 Várnai, T., Marshak, A., and Einaudi, F.: Influence of 3D Radiative Effects on Satellite Retrievals of Cloud
 948 Properties, 2001.

949 Várnai, T.: Influence of Three-Dimensional Radiative Effects on the Spatial Distribution of Shortwave
 950 Cloud Reflection, Journal of the Atmospheric Sciences, 57, 216-229,
 951 [https://doi.org/10.1175/1520-0469\(2000\)057<0216:IOTDRE>2.0.CO;2](https://doi.org/10.1175/1520-0469(2000)057<0216:IOTDRE>2.0.CO;2), 2000.

952 Várnai, T. and Davies, R.: Effects of Cloud Heterogeneities on Shortwave Radiation: Comparison of Cloud-
 953 Top Variability and Internal Heterogeneity, Journal of the Atmospheric Sciences, 56, 4206-4224,
 954 [https://doi.org/10.1175/1520-0469\(1999\)056<4206:EOCHOS>2.0.CO;2](https://doi.org/10.1175/1520-0469(1999)056<4206:EOCHOS>2.0.CO;2), 1999.

955 Várnai, T. and Marshak, A.: Observations of Three-Dimensional Radiative Effects that Influence MODIS
 956 Cloud Optical Thickness Retrievals, Journal of the Atmospheric Sciences, 59, 1607-1618,
 957 [https://doi.org/10.1175/1520-0469\(2002\)059<1607:OOTDRE>2.0.CO;2](https://doi.org/10.1175/1520-0469(2002)059<1607:OOTDRE>2.0.CO;2), 2002.

958 Várnai, T. and Marshak, A.: View angle dependence of cloud optical thicknesses retrieved by Moderate
 959 Resolution Imaging Spectroradiometer (MODIS), Journal of Geophysical Research: Atmospheres,
 960 112, <https://doi.org/10.1029/2005JD006912>, 2007.

961

962 Welch, R. M. and Wielicki, B. A.: Stratocumulus Cloud Field Reflected Fluxes: The Effect of Cloud Shape,
 963 Journal of Atmospheric Sciences, 41, 3085-3103, [https://doi.org/10.1175/1520-0469\(1984\)041<3085:SCFRFT>2.0.CO;2](https://doi.org/10.1175/1520-0469(1984)041<3085:SCFRFT>2.0.CO;2), 1984.

964
 965 Wielicki, B. A., Barkstrom, B. R., Harrison, E. F., Lee, R. B., Smith, G. L., and Cooper, J. E.: Clouds and the
 966 Earth's Radiant Energy System (CERES): An Earth Observing System Experiment, Bulletin of the
 967 American Meteorological Society, 77, 853-868, [https://doi.org/10.1175/1520-0477\(1996\)077<0853:CATERE>2.0.CO;2](https://doi.org/10.1175/1520-0477(1996)077<0853:CATERE>2.0.CO;2), 1996.

968
 969

970 Zelinka, M. D., Klein, S. A., and Hartmann, D. L.: Computing and Partitioning Cloud Feedbacks Using Cloud
971 Property Histograms. Part II: Attribution to Changes in Cloud Amount, Altitude, and Optical
972 Depth, *Journal of Climate*, 25, 3736-3754, <https://doi.org/10.1175/JCLI-D-11-00249.1>, 2012.

973 Zhang, Z. and Platnick, S.: An assessment of differences between cloud effective particle radius retrievals
974 for marine water clouds from three MODIS spectral bands, *Journal of Geophysical Research:*
975 *Atmospheres*, 116, <https://doi.org/10.1029/2011JD016216>, 2011.

976 Zhang, Z., Ackerman, A. S., Feingold, G., Platnick, S., Pincus, R., and Xue, H.: Effects of cloud horizontal
977 inhomogeneity and drizzle on remote sensing of cloud droplet effective radius: Case studies
978 based on large-eddy simulations, *Journal of Geophysical Research: Atmospheres*, 117,
979 <https://doi.org/10.1029/2012JD017655>, 2012.

980 Zhang, Z., Dong, X., Xi, B., Song, H., Ma, P.-L., Ghan, S. J., Platnick, S., and Minnis, P.: Intercomparisons of
981 marine boundary layer cloud properties from the ARM CAP-MBL campaign and two MODIS cloud
982 products, *Journal of Geophysical Research: Atmospheres*, 122, 2351-2365,
983 <https://doi.org/10.1002/2016JD025763>, 2017.

984 Zhang, Z., Werner, F., Cho, H. M., Wind, G., Platnick, S., Ackerman, A. S., Di Girolamo, L., Marshak, A., and
985 Meyer, K.: A framework based on 2-D Taylor expansion for quantifying the impacts of subpixel
986 reflectance variance and covariance on cloud optical thickness and effective radius retrievals
987 based on the bispectral method, *Journal of Geophysical Research: Atmospheres*, 121, 7007-7025,
988 <https://doi.org/10.1002/2016JD024837>, 2016.

989 Zhuravleva, T. B., Kabanov, D. M., Sakerin, S. M., and Firsov, K. M.: Simulation of aerosol direct radiative
990 forcing under typical summer conditions of Siberia. Part 1. Method of calculation and choice of
991 input parameters, *Atmospheric and Oceanic Optics*, 22, 63-73,
992 <https://doi.org/10.1134/S1024856009010102>, 2009.

993
994
995
996
997